



universität  
wien

# DIPLOMARBEIT

Titel der Diplomarbeit

**Analysis of Lidar Wind Measurements at the Bruck an der  
Leitha Wind Park**

Verfasserin

Valerie-Marie Kumer

angestrebter akademischer Grad

Magistra der Naturwissenschaften (Mag.rer.nat)

Wien, 2012

Studienkennzahl: A 415

Studienrichtung: Diplomstudium Meteorologie

Betreuerin: Univ.-Prof. Dr. Vanda Grubišić

# Contents

<b>Abstract</b>	<b>X</b>
<b>Kurzfassung</b>	<b>XI</b>
<b>1 Introduction</b>	<b>1</b>
1.1 Wind Energy . . . . .	1
1.1.1 Historical Overview . . . . .	1
1.1.2 Wind Speed Measurements . . . . .	3
1.1.3 Wind Power . . . . .	4
1.2 Boundary Layer . . . . .	6
1.2.1 Structure of the Boundary Layer . . . . .	6
1.2.2 Governing Equations . . . . .	9
1.2.3 Mathematical Description of Turbulence . . . . .	11
1.2.4 Winds in the PBL . . . . .	15
1.3 LIDAR . . . . .	18
1.3.1 LIDAR Setup . . . . .	18
1.3.2 LIDAR Equation . . . . .	18
1.3.3 LIDAR Techniques . . . . .	21
<b>2 Methods and Data</b>	<b>27</b>



2.1	WINDCUBE <sup>TM</sup> . . . . .	27
2.1.1	Measurement Principle . . . . .	27
2.1.2	Performance . . . . .	28
2.1.3	Data Structure . . . . .	30
2.1.4	Data Accuracy and Availability . . . . .	32
2.2	Wind Vector Reconstruction . . . . .	35
2.2.1	WINDCUBE <sup>TM</sup> . . . . .	35
2.2.2	New Meteorological Reconstruction . . . . .	37
2.3	Measurement Campaign . . . . .	41
2.3.1	Location . . . . .	41
2.3.2	Time Period and Setup . . . . .	43
2.4	TKE Calculation . . . . .	44
<b>3</b>	<b>Results and Discussion</b>	<b>47</b>
3.1	Observed Frequency of Wind Directions . . . . .	48
3.2	Weather classifications . . . . .	51
3.2.1	Synoptic Weather Summary . . . . .	53
3.3	Case studies . . . . .	54
3.3.1	Northwesterly (NW) Case . . . . .	56
3.3.2	Easterly (E) Case . . . . .	59
3.3.3	Southeasterly (SE) Case . . . . .	63
3.3.4	Northerly (N) Case . . . . .	67
3.3.5	Comparison of the Case Studies . . . . .	70
<b>4</b>	<b>Conclusion</b>	<b>73</b>

Appendix	78
Acknowledgments	83
Curriculum Vitae	85

# List of Figures

1.1	First wind turbine, designed and built by Charles Brush in 1888. . . .	2
1.2	Structure of the atmospheric boundary layer from Stull (1991). . . . .	7
1.3	Logarithmic wind profiles dependent on atmospheric condition (Tong, 2010) . . . . .	17
1.4	LIDAR geometry (Weitkamp, 2005) . . . . .	20
1.5	Principle of a heterodyne detection (Weitkamp, 2005) . . . . .	24
2.1	WINDCUBE <sup>TM</sup> sample volume (LEOSPHERE, 2008) . . . . .	28
2.2	Relative absorption of radiation by the atmosphere as a function of the wavelength. The dashed line indicates the wavelength of the WINDCUBE <sup>TM</sup> laser. (Mayer, 2009) . . . . .	29
2.3	Availability of turbulence processed data in % . . . . .	32
2.4	Correlation between data gaps and a CNR < -20dB . . . . .	33
2.5	Correlation between data availability and wiper activity . . . . .	33
2.6	High resolution visible cloud image on red and green channel . . . . .	34
2.7	Orthogonal frame of the WINDCUBE <sup>TM</sup> for retrieving the wind components (LEOSPHERE, 2008) . . . . .	35
2.8	Comparison between the meteorological orthogonal frame and that of the WINDCUBE <sup>TM</sup> . . . . .	36

2.9	Bottom: 10 min vertical wind profiles of 17 UTC on September 5 <sup>th</sup> for the meteorological coordinate system (left) and for the system of the WINDCUBE <sup>TM</sup> (right). Top: 10 m wind streamlines calculated with the analysis tool VERA at 17 UTC and wind barbs at 925 hPa calculated with the GFS analysis at 18 UTC . . . . .	37
2.10	Orthogonal frame for retrieving the meteorologically defined wind components . . . . .	38
2.11	Topography of Eastern Austria . . . . .	41
2.12	Topography of Bruck and the surrounding area . . . . .	42
2.13	Wind park location (Bourgeois, 2010) . . . . .	43
2.14	Polynomial fit of the horizontal wind speed at 06 and 12 UTC October 4 <sup>th</sup> , 2010. . . . .	45
2.15	Energy spectrum of the horizontal wind speed calculated for each measurement height. The red lines indicate the frequency of a day, a hour and a minute respectively. . . . .	46
3.1	Total time series of the horizontal wind speed at 65 m (green line) and 200 m (blue line) measured by the WINDCUBES WLS7-70 and WLS7-85 . . . . .	47
3.2	Wind roses from the Bruck an der Leitha wind park for the period of 26.8.2010-6.10.2010 with horizontal wind speeds greater than 3 m/s .	48
3.3	Wind rose at 65 m overlaid with the topography of the surrounding area	49
3.4	Mean wind field of the region of the Alps from 1980 until 2001 (Lotteraner, 2009) . . . . .	50
3.5	Wind direction frequencies for all wind speeds. . . . .	50
3.6	Wind rose at 65 m for wind speeds greater than 3 m/s . . . . .	50
3.7	Wind direction frequencies for wind speeds grater than 3 <i>m/s</i> . . . . .	50

3.8	Surface pressure and 500hPa geopotential distribution over Central Europe from GFS at 12 UTC September 1 <sup>st</sup> , 2010. . . . .	56
3.9	Streamlines of 10 m wind and potential temperature from VERA at 12 UTC September 1 <sup>st</sup> , 2010. . . . .	56
3.10	vertical wind profile (right) on September 1 <sup>st</sup> . . . . .	57
3.11	Vertical profiles of horizontal wind speed [m/s] and TKE [ $m^2s^{-2}$ ] on September 1 <sup>st</sup> , 2010. . . . .	57
3.12	Profile of shear generation, vertical advection and tendency of the TKE budget on September 1 <sup>st</sup> at 12 UTC. . . . .	58
3.13	Surface pressure and 500 hPa geopotential distribution over Central Europe from GFS at 12 UTC September 25 <sup>th</sup> , 2010. . . . .	59
3.14	Streamlines of 10 m wind and potential temperature from VERA at 12 UTC September 25 <sup>th</sup> , 2010. . . . .	59
3.15	Wind profile of September 25 <sup>th</sup> , 2010. . . . .	60
3.16	Vertical profiles of wind direction [°], horizontal wind speed [m/s] and TKE [ $m^2s^{-2}$ ] on September 25 <sup>th</sup> , 2010 . . . . .	60
3.17	Location of the WINDCUBE <sup>TM</sup> in the wake downstream of the wind turbine WEA 4 . . . . .	61
3.18	Profiles of the wind components u, v, w [m/s] on September 25 <sup>th</sup> , 2010. . . . .	62
3.19	Profiles of horizontal wind speed (left) and shear generation $S$ , vertical advection $AD$ , tendency $T$ of the TKE budget (right) at 06 UTC September 25 <sup>th</sup> , 2010. . . . .	62
3.20	Surface pressure and 500 hPa geopotential distribution over Central Europe from GFS at 12 UTC October 4 <sup>th</sup> , 2010. . . . .	63
3.21	Streamlines of 10 m wind and potential temperature from VERA at 12 UTC October 4 <sup>th</sup> , 2010. . . . .	64

3.22	Vertical wind profile on October 4 <sup>th</sup> , 2010. . . . .	64
3.23	Eumetrain HRVIS satellite images at 12 UTC October 4 <sup>th</sup> , 2010. . . .	64
3.24	Vertical profiles of horizontal wind speed [m/s] and TKE [ $m^2s^{-2}$ ] on October 4 <sup>th</sup> , 2010. . . . .	65
3.25	Profiles of the wind components $u$ , $v$ , $w$ [m/s] on October 4 <sup>th</sup> , 2010. .	66
3.26	Profile of shear generation $S$ , vertical advection $AD$ and tendency $T$ of the TKE budget at 15 UTC October 4 <sup>th</sup> , 2010. . . . .	66
3.27	Surface pressure and 500hPa geopotential distribution over Europe from GFS at 12 UTC September 5 <sup>th</sup> , 2010. . . . .	67
3.28	Streamlines of 10 m wind and potential temperature from VERA at 12 UTC September 5 <sup>th</sup> , 2010. . . . .	68
3.29	Vertical wind profile on September 5 <sup>th</sup> , 2010. . . . .	68
3.30	Vertical profiles of horizontal wind speed [m/s] and TKE [ $m^2s^{-2}$ ] on September 5 <sup>th</sup> , 2010. . . . .	68
3.31	Profile of the vertical wind components $w$ [m/s] on September 5 <sup>th</sup> , 2010.	69
3.32	Time-height cross section for a 1-D simulation over land with the MIUU mesoscale model, for the diurnal cycle of the mean wind speed (Jansson, 2002) . . . . .	69
3.33	TKE profiles and their relation to the total kinetic energy, from case NW at 11 UTC, case N and case SE at 12 UTC and case E at 06 UTC	70
3.34	Turbulence intensity $TI$ at different heights as a function of wind di- rection. . . . .	71
3.35	Monthly weather class frequencies of the four case studies . . . . .	72
4.1	File sample of the rowdata set . . . . .	79
4.2	File sample of the turbulence processed data set . . . . .	80

# List of Tables

2.1	WINDCUBE <sup>TM</sup> characteristics (Aussibal, 2008) . . . . .	30
2.2	WINDCUBE <sup>TM</sup> file structure raw data (Aussibal, 2008) . . . . .	31
2.3	WINDCUBE <sup>TM</sup> file structure turbulence processed data (Aussibal, 2008)	31
2.4	WINDCUBE <sup>TM</sup> data accuracy . . . . .	32
2.5	Location of the WINDCUBE <sup>TM</sup> (Bourgeois, 2010) . . . . .	42
2.6	WINDCUBE <sup>TM</sup> measurement altitudes . . . . .	44
3.1	Weather classes by Heß and Brezowsky . . . . .	52
3.2	Weather classes for the period of analysis by Heß and Brezowsky . . .	53

*"When you want something,  
all the universe conspires in helping you to achieve it."*

*Paulo Coelho*

## Dedication

This thesis is dedicated to my parents, who could not yet finish their studies,  
but made it possible for myself.



# Abstract <sup>1</sup>

Due to the increase in height of the wind turbine masts in recent years, it has become difficult to obtain much needed wind profile measurements via traditional tower measurements. In response to that, there has been an increase in use of remote sensing methods for obtaining wind profiles for wind turbine operation and siting. In this study we analyzed Doppler LIDAR measurements obtained in a field campaign at a wind park operated by VERBUND Renewable Power GmbH and located near Bruck-an-der-Leitha (Lower Austria). A WINDCUBE<sup>TM</sup> Doppler LIDAR, manufactured by Leosphere, was used to collect data over a three-month period.

Given that the top measurement height of 200 m is located inside the atmospheric boundary layer, which has closed to logarithmic wind profile and is turbulent, leads to fluctuations of the wind field having great importance. Due to a sufficiently high sampling rate (0.25 Hz at one out of 4 measurement points) the calculations of variances and covariances of wind parameters are possible using this data set and allow an analysis of derived parameters such as turbulent kinetic energy (TKE).

The characteristics of certain weather patterns and flow fields and their influence on the wind park are of particular interest. This knowledge could lead to improvement of power curve prediction and would aid engineering designs, aimed at prolonging the lifetime of wind turbines. Therefore, kinetic energy and the meteorological parameters, such as wind speed and its components, are analyzed and compared for several case studies, dependent on the wind direction and weather situation.

Results show that the main wind direction is conditioned by topography of the region and is strongly influenced by the flow around the Alps. Dependent on the weather situation different flow characteristics were documented by the measurements, such as wake effects downstream of the wind turbine seen in profiles of horizontal wind speed and TKE. At the site of the Bruck/Leitha wind park, these situations are due to easterly flows corresponding to Vb Cyclone events.

---

<sup>1</sup>Parts of this abstract is published at the homepage of the Department of Meteorology and Geophysics Vienna (IMGW), <http://img.univie.ac.at/en/home/>

# Kurzfassung <sup>2</sup>

Auf Grund der stetig größer werdenden Windkraftanlagen wird es messtechnisch schwieriger, Windprofile mit herkömmlichen meteorologischen Masten zu erfassen. Daher geht der Trend zur Datenbestimmung mittels bodengestützter Fernerkundungssysteme wie SODAR oder LIDAR.

Für diese Studie stehen LIDAR Daten einer Messkampagne von VERBUND Renewable Power GmbH zur Verfügung. Ein WINDCUBE<sup>TM</sup>, hergestellt von Leosphere, wurde über einen Zeitraum von drei Monaten in einem Windpark westlich von Bruck an der Leitha (NÖ) zur Datenaufnahme betrieben. Das Messprinzip dieses Geräts basiert auf der Ermittlung von radialen Windgeschwindigkeiten durch den Dopplereffekt, der bei der Rückstreuung von Lichtimpulsen an Aerosolen zustande kommt.

Die gewonnenen Daten werden in neun verschiedenen Höhengniveaus von 40 bis 200 m über Grund, also innerhalb der atmosphärischen Grenzschicht gemessen. Das Windprofil in dieser Schicht ist nahezu logarithmisch und Turbulenz spielt dabei eine tragende Rolle. Aus einer Messreihe mit einer Datendichte von 0,25 Hz an je einem von vier Punkten kann man diese turbulenten Flüsse berechnen und so abgeleitete Größen wie die turbulente kinetische Energie (TKE) zur Analyse heranziehen.

Der Untersuchungswertpunkt liegt vor allem auf dem Einfluss einzelner Wetterlagen und Strömungsmuster auf die TKE Verteilung. Kenntnisse darüber würden Leistungsvorhersagen verbessern, sowie durch Optimierung der Konstruktion eine höhere Lebensdauer der Windkraftanlage ermöglichen. Im Zuge dessen werden relevante Größen wie Windgeschwindigkeit oder TKE in Fallstudien untersucht, abhängig von der Wetterlage.

Resultate zeigen, dass die Hauptwindrichtungen durch die Topographie der Region gegeben sind und stark im Zusammenhang mit der Umströmung der Alpen stehen. Bei Ostwinden, bedingt durch eine Vb-artige Wetterlage, sind stromabwärts der Windkraftanlage Verwirbelungen im TKE-Profil sowie ein Rückgang der horizontalen Windgeschwindigkeit zu erkennen.

---

<sup>2</sup>Teile davon wurden innerhalb des 4. Österreichischen Meteorologentags 2011 veröffentlicht

# Chapter 1

## Introduction

### 1.1 Wind Energy

Wind energy describes the conversion of kinetic energy of air flow, first into mechanic energy and subsequently into electricity, that goes either directly into consumption or into an electrical grid. This conversion is carried out by wind turbines of different sizes, either on land or offshore, leading to an output power ranging from a few kW up to 10 MW. Wind energy is one of the rising branches of energy generation due to its pollutant free production and to its unlimited resource, the flow of the atmosphere (Tong, 2010).

#### 1.1.1 Historical Overview

The idea of utilization of wind power has been in existence for a long time, from when the ancient Chinese attached sails to their rafts around 4000 BC and when later, around 3400 BC, the ancient Egyptians launched their first sailing vessels to sail on the Nile River. Until the invention of steam engines in the 19th century, wind was the main driving force for boats.

Almost as far back reaches the history of windmills shown in mural paintings of the late Eastern Han Dynasty (25-220 AD) in China. Vertical axis windmills were invented by the Persians for grinding grain and for pumping water in the ninth century, while horizontal axis windmills were first built in northwestern Europe in

the 1180s. The first wind turbine that converted wind energy into electricity was designed and built by Charles Brush in 1888 in the United States of America to charge batteries. It consisted of 144 cedar blades with a rotor diameter of 17 m seen in figure 1.1. That wind turbine generated a peak power of 12 kW.

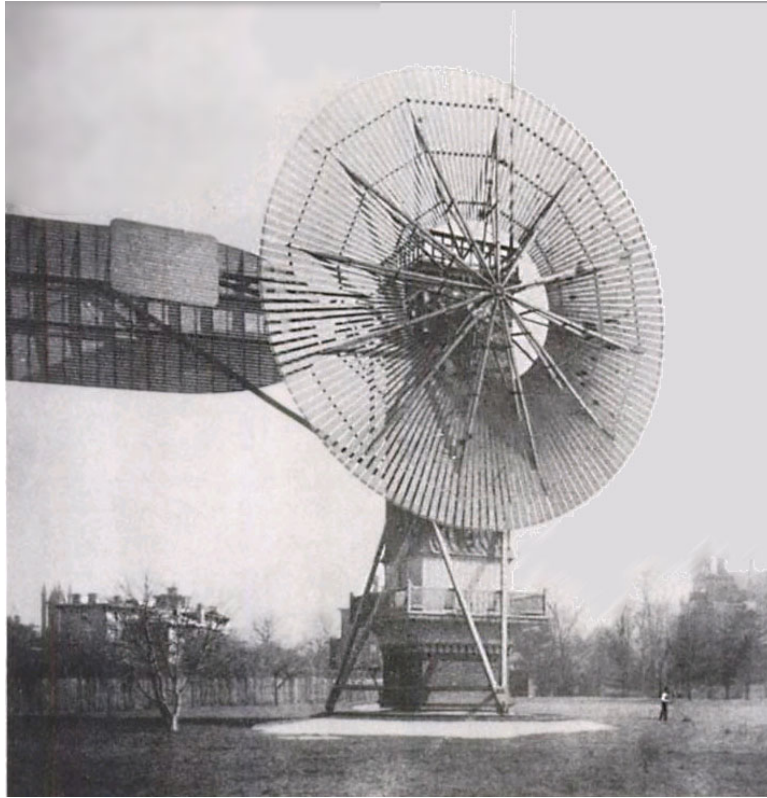


Figure 1.1: First wind turbine designed and built by Charles Brush in 1888. <sup>1</sup>

The first wind turbine that had a similar design to modern wind turbines was constructed in Denmark in the mid 1950s and had three blades mounted on a horizontal rotation axis. Nowadays wind turbines can generally be classified according to their capacity, according to their design as vertical or horizontal axis wind turbines, or according to their position on shore or off shore.

---

<sup>1</sup>Source: [http://upload.wikimedia.org/wikipedia/commons/5/55/Wind\\_turbine\\_1888\\_Charles\\_Brush.jpg](http://upload.wikimedia.org/wikipedia/commons/5/55/Wind_turbine_1888_Charles_Brush.jpg), last accessed on January 23, 2012.

### 1.1.2 Wind Speed Measurements

The importance of wind in the generation of electricity via wind turbines is already emphasized in the term "wind energy" itself. When building a new wind park or conducting research in an existing wind park, it is of utmost importance to be familiar to the wind climatology of the site. Hence, meteorological measurements and data evaluation, in form of models designed to reflect, e.g. the local climate conditions, are indispensable.

As a first step, the reanalysis data - a time series of meteorological parameters from the past obtained from a grid of synoptic weather stations world wide - is combined with a topographical map in order to make a prediction of the wind fields climatological average. Further, in-situ wind measurement data is collected, normally for the minimum period of a few years, in order to prevent sub- and interannual deviations. It should, however, represent a 50 years average value of the wind speed.

Measurements can be taken either with mechanical cup or propeller anemometers, with ultrasonic anemometers or, as a new trend, with ground-based remote sensing devices. Because the wind information at the hub height is crucial, the anemometers have to be installed on a so-called meteorological mast. This can be challenging not only in terms of construction, but also considering possible shadowing effects. An alternative to the construction of a meteorological mast are ground based remote sensing devices that measure wind speeds at several heights and are easy to handle. Although at present, they have some disadvantages, in particular regarding costs and energy consumption, the remote-sensing devices will be of growing importance in the future.

Besides a wind climatology, information about the orography, the roughness of the terrain and information regarding obstacles are put together in a wind atlas. This atlas is normally produced with Wind Atlas Analysis and Application Program (*WAsP*), a micro scale model that forms a good base for further investigations in building a new wind park. (Tong, 2010)

### 1.1.3 Wind Power

With the knowledge of the wind climatology of a specific region, one can start thinking about how to utilize energy of the prevailing winds. The most important factor in this is nicely illustrated in the equation of physical power, which describes the rate of transferred kinetic energy in the area of interest. In fact, it gives information on how much mechanical work can be produced in a specific time frame by wind turbine that later will be transferred onto the electricity grid in order to, for example, supply a city. The kinetic energy is defined as

$$E_{KIN} = \frac{mv^2}{2}, \quad (1.1)$$

where  $v$  is the mean wind speed and  $m$  the mass of air. Taking the derivative of the kinetic energy with respect to time, and replacing the mass flow by its definition, leads to the physical power  $P$

$$P = \frac{dE_{KIN}}{dt} = \frac{1}{2} \frac{dm}{dt} v^2 \quad \text{with} \quad \frac{dm}{dt} = \rho v A \quad (1.2)$$

$$P = \frac{\rho A v^3}{2}. \quad (1.3)$$

As one can see in equation 1.3 the wind power is directly proportional to the area of the cross-section  $A$  of the wind turbine, thus to the diameter of the rotor blades, and to air density  $\rho$ . Of importance is also the fact that wind speed is included in the power calculation with the cubic power. Thus, little differences in the wind speed can have a huge impact on the output power, which makes the power forecast difficult and sensitive to the predicted wind field.

The so-called power curve is the relation between the wind speed and the physical power of the wind. The higher the wind speed the greater the power that one can get. But, there is an upper limit to this. At a certain wind speed, called the cut-off wind speed, the wind turbine needs to be turned off because it no longer produces

useful power, also, to prevent damage to the turbine. A counterpart to the cut-off wind speed is a cut-in wind speed, defined as that wind speed at which the wind turbine starts producing more power than it is needed for its operation. These two thresholds are constant values dependent on the type of the wind turbine. In this context, the wind speed always means the wind speed at the hub height.

In reality there are a few more parameters that influence the power curve, such as the power coefficient  $C_p$ , which relates the actually captured mechanical power to the available wind power (Tong, 2010). Energy losses through the mechanical momentum on the rotor, as well as through the energy conversion in the electronic inverter are included in the system efficiency  $\eta_s$  (Hofstetter, 2011). The effective output power of the wind turbine  $P_{eff}$  can, with respect to the total efficiency  $\eta_t$ , be written as follows

$$\eta_t = C_p \eta_s \quad \text{with} \quad C_p = \frac{P_{out}}{P_w} \quad (1.4)$$

$$P_{eff} = \frac{\eta_t \rho A v^3}{2}. \quad (1.5)$$

The power curves are usually determined by field measurements. As the wind information at a site is an essential factor in power calculations and forecasts, further research is needed for improving wind measurements and forecasts (Hofstetter, 2011).

## 1.2 Boundary Layer

As wind turbines are on average about one hundred meters high, the surrounding air lies within the atmospheric boundary layer, that has a depth between 10 and 3000 meters. Stull (1991) defines the boundary layer as the part of the troposphere that is directly influenced by the earth's surface and that responds to surface forcing within a timeframe of an hour or less.

### 1.2.1 Structure of the Boundary Layer

Over land and in high pressure weather situations the planetary boundary layer (PBL) has a well defined structure that exhibits a diurnal cycle. This diurnal variation is due to temperature changes primarily caused by transport of heat from the ground into the lower atmosphere during the day and also to a small fraction by absorption of solar radiation. In the free atmosphere these effect are significantly weaker and the temperature is controlled by other processes. The PBL seen over land comprises of three main layers (Figure 1.2), the *Stable Boundary Layer*, the *Mixed Layer* and the *Residual Layer*.

As two of the main surface forcings representative in the PBL are frictional drag and heat transfer, it is obvious that turbulence is the dominant part regarding the motion of air in that layer of the atmosphere. According to Stull (1991), turbulence can be visualized as consisting of irregular swirls of motion of different sizes called eddies, superimposed on each other.

Before going into detail in describing the different layers of the PBL, it is helpful to shortly introduce three different atmospheric conditions that can indicate possible regimes regarding atmospheric movements. A small vertical displacement of an air parcel can be described mathematically as the following

$$\frac{D^2}{Dt^2}(\delta z) = -N^2\delta z, \quad \text{where} \quad N^2 = \frac{g}{\theta_0} \frac{d\theta_0}{dz} \quad (1.6)$$



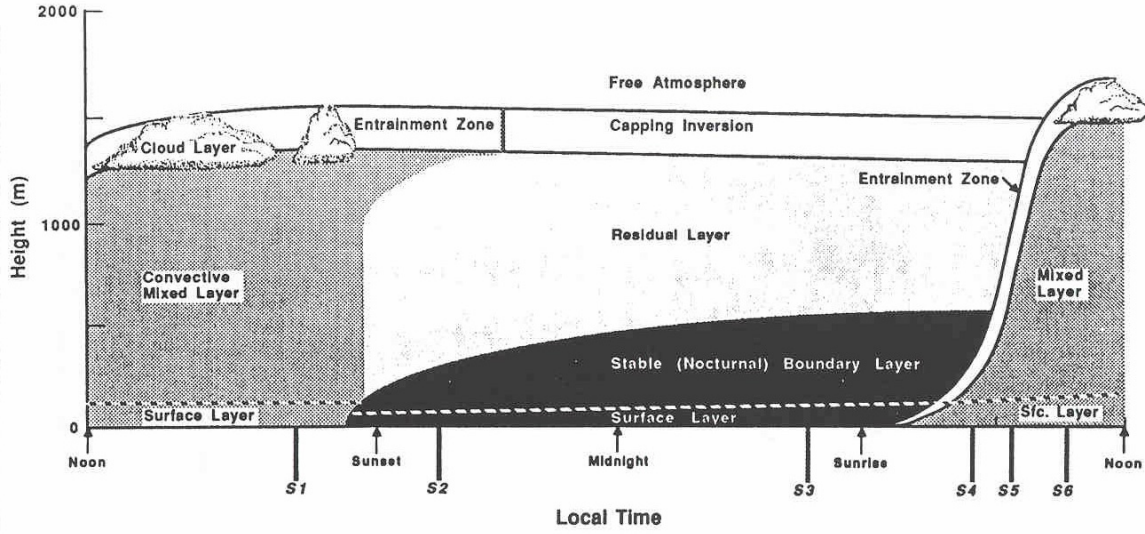


Figure 1.2: Structure of the atmospheric boundary layer from Stull (1991).

is the Brunt-Väisälä frequency or buoyancy frequency,  $\delta z$  is the vertical displacement,  $g$  the magnitude of gravity and  $\theta_0$  the basic state potential temperature of the air parcel. The potential temperature is the temperature that a parcel of dry air at a certain pressure  $p$  and temperature  $T$  would have, if it was adiabatically moved to the standard pressure  $p_s$

$$\theta = T \left( \frac{p_s}{p} \right)^{\frac{R}{c_p}}, \quad (1.7)$$

where  $R$  is the gas constant for dry air and  $c_p$  is the specific heat of dry air at constant pressure. Therefore, the buoyancy frequency  $N^2$  is a measure for static stability (Holton, 2004). The solution of equation 1.6  $\delta z = A \exp(iNt)$  leads to the following

$N^2 > 0$	air parcel oscillates around its initial state
$N^2 < 0$	exponentially increasing displacement
$N^2 = 0$	no acceleration

### **Stable Stratification of the Atmosphere**

In a statically stable stratification of the atmosphere, potential temperature  $\theta_0$  has to increase with height ( $\frac{\partial\theta_0}{\partial z} > 0$ ). Consequently a vertically displaced air parcel will always go back to its equilibrium state, which means that no mixing occurs. This is typically the case in high pressure situations with low wind speeds in wintertime or during night.

### **Unstable Stratification of the Atmosphere**

The converse atmospheric condition is an unstable stratification where either through solar radiation or cold air advection potential temperature  $\theta_0$  decreases with height ( $\frac{\partial\theta_0}{\partial z} < 0$ ). That means heated ground or the air near the ground is warmer than air higher up. This induces a thermally driven circulation that leads to a vertical mixing of the whole PBL. The mixing can be described through turbulent heat and momentum transfer, with a depth depending on the time of the year.

### **Neutral Stratification of the Atmosphere**

If the atmosphere is under neutral condition, potential temperature  $\theta_0$  does not change with height ( $\frac{\partial\theta_0}{\partial z} = 0$ ). If there is no vertical displacement, e.g. due to orography, the air parcel will stay in its initial position. This constant mixed layer normally occurs with higher wind speeds, resulting in a temperature drop of 1 K per 100 m.

### **Mixed Layer**

The main characteristic of the *Mixed Layer (ML)* is that it is usually built by convectively driven turbulence, which leads, as described above, to mixing of air at different heights that can be seen in a constant potential temperature profile. Depth of ML depends on the season due to different intensity of convection which leads to greater temperature difference between an air parcel and its surrounding that can be obtained mostly by strong solar radiation or strong cold air advection at higher altitudes. A

nearly well-mixed layer can also form if there are sufficiently strong winds, for example during the passage of a frontal system. Turbulence generated by vertical wind shear on top of the ML is one form of clear air turbulence (CAT).

### Residual Layer

As the sun sets, the thermal driver for turbulence closes to exist and turbulence decays, assuming that there is no cold air advection. The resulting layer is the *Residual Layer (RL)*. It has the same initial conditions as the mixed layer, regarding no cold air advection and is neutrally stratified.

### Stable Boundary Layer

Underneath the RL, the *Stable Boundary Layer (SBL)* forms during night time. This layer is characterized by stable atmospheric conditions, resulting from cooling of the air near ground and very weak winds. The formation of the SBL leads to a separation of RL from the surface. Therefore, friction plays no longer a role in the RL and an imbalance between friction and the pressure gradient force forms, resulting in an acceleration of the wind above the SBL. Wind speeds higher than the geostrophic wind, which is parallel to the isobars, can occur and are called *nocturnal low-level wind maximum*. The formation of a *low-level-jet* is also possible through synoptic-scale dynamics but is not related to the diurnal cycle in the PBL (Richardson, 2010).

## 1.2.2 Governing Equations

To consider turbulence in a mathematical way state variables  $\chi$  are split into a slowly in time varying mean part  $\bar{\chi}$  and a perturbation part  $\chi'$

$$\chi = \bar{\chi} + \chi', \quad (1.8)$$

with  $\bar{\chi}$  being the arithmetic time mean

$$\bar{\chi} = \frac{1}{N} \sum_{i=1}^N \chi_i, \quad (1.9)$$

where  $N$  is the end of the considered time span and  $\chi_i$  is the state variable at time  $i$ . Accounting for the presence of turbulence one must account the transfer of momentum, heat and moisture by eddies in the dynamic equations to represent the meteorological fields in the PBL as good as possible (Richardson, 2010). One should also keep in mind that friction is a dominant force in the PBL and can't be neglected in retrieving the governing equations of motion. Thus, the momentum equations in the PBL are:

$$\frac{\partial u}{\partial t} = -u \frac{\partial u}{\partial x} - v \frac{\partial u}{\partial y} - w \frac{\partial u}{\partial z} - \frac{1}{\rho_0} \frac{\partial p}{\partial x} + f v + \nu \nabla^2 u \quad (1.10)$$

$$\frac{\partial v}{\partial t} = -u \frac{\partial v}{\partial x} - v \frac{\partial v}{\partial y} - w \frac{\partial v}{\partial z} - \frac{1}{\rho_0} \frac{\partial p}{\partial y} - f u + \nu \nabla^2 v \quad (1.11)$$

$$\frac{\partial w}{\partial t} = -u \frac{\partial w}{\partial x} - v \frac{\partial w}{\partial y} - w \frac{\partial w}{\partial z} - \frac{1}{\rho_0} \frac{\partial p}{\partial z} - g - \frac{\rho'}{\rho_0} g + \nu \nabla^2 w \quad (1.12)$$

where  $u, v, w$  are the three-dimensional wind components,  $\rho_0$  is a constant reference density,  $p$  is the local pressure,  $f$  is the Coriolis parameter,  $\nu$  is the kinematic viscosity, and  $x, y, z$  represent the spatial coordinates.

The representative terms of the equations 1.10 - 1.12 are advection ( $-\vec{u} * \nabla \vec{u}$ ), the pressure gradient force ( $-\frac{1}{\rho_0} \frac{\partial p}{\partial x}, -\frac{1}{\rho_0} \frac{\partial p}{\partial y}, -\frac{1}{\rho_0} \frac{\partial p}{\partial z}$ ), the Coriolis force and friction respectively and without the Coriolis term are called Navier-Stokes momentum equations. In order to simplify these equations the Boussinesq approximation is applied, which means that density everywhere has constant value  $\rho_0$ , except in the buoyancy term in the vertical momentum equation (Holton, 2004).

Applying the Reynolds average on equations 1.10 - 1.12 while assuming that the product of the perturbations and the mean vanishes when the average is taken, leads to

$$\frac{\partial \bar{u}}{\partial t} = -\bar{u} \frac{\partial \bar{u}}{\partial x} - \bar{v} \frac{\partial \bar{u}}{\partial y} - \bar{w} \frac{\partial \bar{u}}{\partial z} - \frac{1}{\rho_0} \frac{\partial \bar{p}}{\partial x} + f\bar{v} + \nu \nabla^2 \bar{u} - \frac{\partial \overline{u'u'}}{\partial x} - \frac{\partial \overline{u'v'}}{\partial y} - \frac{\partial \overline{u'w'}}{\partial z} \quad (1.13)$$

$$\frac{\partial \bar{v}}{\partial t} = -\bar{u} \frac{\partial \bar{v}}{\partial x} - \bar{v} \frac{\partial \bar{v}}{\partial y} - \bar{w} \frac{\partial \bar{v}}{\partial z} - \frac{1}{\rho_0} \frac{\partial \bar{p}}{\partial y} - f\bar{u} + \nu \nabla^2 \bar{v} - \frac{\partial \overline{v'u'}}{\partial x} - \frac{\partial \overline{v'v'}}{\partial y} - \frac{\partial \overline{v'w'}}{\partial z} \quad (1.14)$$

$$\frac{\partial \bar{w}}{\partial t} = -\bar{u} \frac{\partial \bar{w}}{\partial x} - \bar{v} \frac{\partial \bar{w}}{\partial y} - \bar{w} \frac{\partial \bar{w}}{\partial z} - \frac{1}{\rho_0} \frac{\partial \bar{p}}{\partial z} - g + \nu \nabla^2 \bar{w} - \frac{\partial \overline{w'u'}}{\partial x} - \frac{\partial \overline{w'v'}}{\partial y} - \frac{\partial \overline{w'w'}}{\partial z}. \quad (1.15)$$

Equations 1.13 - 1.15 are the Reynolds-averaged Navier-Stokes equations or short Reynolds equations. These equations lay the foundation for analyses in the boundary layer meteorology.

### 1.2.3 Mathematical Description of Turbulence

Turbulence can either be described by the equations of motions that were derived in section 1.2.2, leading to the definition of turbulent kinetic energy, or by a statistical analysis of time series of wind speed, treating turbulence as the perturbation of the mean flow. Both ways allow one to make a statement on turbulence intensity by analyzing wind data. Considering the dynamics of the atmosphere by using the momentum equations it is even possible to predict the turbulent kinetic energy as we will see later on.

#### Statistical description

According to Cebeci (2004) turbulence  $T_i$  is seen as a perturbation of the mean flow. It can be written in terms of the wind speed as

$$T_i = u'_i = u_i - \bar{u}, \quad (1.16)$$

where  $\bar{u}$  is the mean wind speed and  $u_i$  is the wind speed at time  $i$ .

As the focus is on a representative measure of turbulence over a certain period of time one has to consider the average. The normal average of  $T_i$  would be zero but

this is not the case for the root mean square

$$RMS = \sqrt{\frac{1}{N} \sum_{i=0}^{N-1} T_i^2}. \quad (1.17)$$

By inserting equation 1.16 into equation 1.17 one can see that the RMS of the perturbation is equal to the standard deviation  $\sigma$  of the wind speed.

$$RMS = \sqrt{\frac{1}{N} \sum_{i=0}^{N-1} (u_i - \bar{u})^2} = \sigma(u) \quad (1.18)$$

The standard deviation of the wind speed is thus a measure for the velocity fluctuations and is called turbulence intensity  $TI$ . It is often expressed as a relative intensity, relating to the mean wind speed

$$TI = \frac{\sigma(u)}{\bar{u}}. \quad (1.19)$$

### Dynamical description

By splitting motion into a mean and a perturbation part, it is also possible to split the energy of the flow into the mean and the perturbation part. With the average and the perturbation of the kinetic energy  $e$  the mean kinetic energy  $\bar{e}$  and the turbulent kinetic energy  $e'$  are defined in the following way:

$$e = \frac{1}{2}(u^2 + v^2 + w^2), \quad (1.20)$$

$$\bar{e} = \frac{1}{2}(\overline{u^2} + \overline{v^2} + \overline{w^2}), \quad (1.21)$$

$$e' = \frac{1}{2}(u'^2 + v'^2 + w'^2). \quad (1.22)$$

Hence another measure for the turbulence intensity becomes the mean turbulent kinetic energy that will from now on be referred to as turbulent kinetic energy  $TKE$ .

$$TKE = \bar{e'} = \frac{1}{2}(\overline{u'^2} + \overline{v'^2} + \overline{w'^2}) \quad (1.23)$$

On the basis of the momentum equations, which provide information on how the wind components change with time, it is possible to calculate the tendency of TKE. Equation 1.24 represents this TKE tendency equation, which allows forecasting of TKE values. It will be easier to understand further steps if one looks at one term of the TKE definition in equation 1.23, e.g.  $\overline{u'^2}$ . That term represents the perturbation of the zonal wind component multiplied by itself and Reynolds averaged. To retrieve this term three steps are applied on the zonal momentum equation. The first step is to find the equation for the tendency of the perturbed wind component, which is done by subtracting the averaged momentum equation 1.13 from its normal form (equation 1.10). In the second step the perturbation tendencies are multiplied with perturbed wind component  $u'$ . The final step is to Reynolds average this equation. To get the final prognostic equation for TKE the Reynolds averaged equations for  $\frac{\partial \overline{u'^2}}{\partial t}$ ,  $\frac{\partial \overline{v'^2}}{\partial t}$ ,  $\frac{\partial \overline{w'^2}}{\partial t}$  have to be summed

$$\begin{aligned}
 \underbrace{\frac{\partial TKE}{\partial t}}_{\text{Tendency}} = & \underbrace{-\bar{u} \frac{\partial TKE}{\partial x} - \bar{v} \frac{\partial TKE}{\partial y} - \bar{w} \frac{\partial TKE}{\partial z}}_{\text{Advection}} + \underbrace{\frac{g}{\theta} \overline{w'\theta'}}_{\text{Buoyancy generation/consumption}} + \\
 & \underbrace{-\overline{u'u'} \frac{\partial \bar{u}}{\partial x} - \overline{v'u'} \frac{\partial \bar{v}}{\partial x} - \overline{w'u'} \frac{\partial \bar{w}}{\partial x} - \overline{u'v'} \frac{\partial \bar{u}}{\partial y} - \overline{v'v'} \frac{\partial \bar{v}}{\partial y} - \overline{w'v'} \frac{\partial \bar{w}}{\partial y} - \overline{u'w'} \frac{\partial \bar{u}}{\partial z} - \overline{v'w'} \frac{\partial \bar{v}}{\partial z} - \overline{w'w'} \frac{\partial \bar{w}}{\partial z}}_{\text{Shear generation}} + \\
 & \underbrace{-\frac{\partial \overline{u'TKE}}{\partial x} - \frac{\partial \overline{v'TKE}}{\partial y} - \frac{\partial \overline{w'TKE}}{\partial z}}_{\text{Turbulent transport}} + \\
 & \underbrace{-\frac{1}{\rho_0} \frac{\partial \overline{u'p'}}{\partial x} - \frac{1}{\rho_0} \frac{\partial \overline{v'p'}}{\partial y} - \frac{1}{\rho_0} \frac{\partial \overline{w'p'}}{\partial z}}_{\text{Pressure correlation}} \underbrace{-\epsilon}_{\text{Dissipation}}. \tag{1.24}
 \end{aligned}$$

This is a powerful equation that provides useful information on the origin of TKE. The first term on the left-hand-side of the equation is the local tendency or storage

of TKE. The sum of the tendency and the advection terms represents the total rate of change of TKE. With all the remaining terms on the right-hand-side of the equation 1.24 the total rate of change of TKE is non zero. This shows that TKE is not a conserved physical quantity; instead, a number of physical processes can lead to generation and dissipation of TKE. One of these processes is the buoyant production of TKE, with its most important term  $\overline{w'\theta'}$  - the so-called turbulent vertical heat flux. This term acts only on the vertical component of TKE. Therefore, this term is largest on convective days, being much stronger on these days compared to cloudy days or even to days with statically stable conditions.

Another TKE generation mechanism is mechanical production by wind shear. This term is largest near the ground due to loss of momentum caused by friction. A smaller maximum of shear generation is found on top of the mixed layer where wind speed approaches its geostrophic value, leading to the already mentioned clear air turbulence. The most important terms of the shear generation are  $\overline{u'w'}\frac{\partial \bar{u}}{\partial z}$  and  $\overline{v'w'}\frac{\partial \bar{v}}{\partial z}$  because greatest vertical shears are associated with a change in the horizontal wind components with height. Therefore the shear generation term mainly produces turbulence in the horizontal direction compared to the buoyant production that acts in the vertical direction.

The main sink of turbulence is its dissipation, the loss of energy on the molecular scale, which is greatest for small sized eddies. Typically, the larger the TKE the larger the dissipation rate; although the sinks and sources in the TKE equation are not perfectly balanced due to the fact that there are also transport terms in the TKE budget. These transport terms include turbulent transport, which represents moving of TKE around by turbulent eddies, and advection, that delivers the TKE generated from somewhere else or brings less turbulent air into the considered area.

The last term that closes the discussed TKE budget is the pressure correlation term, which is typically calculated as the residual from all the other terms, because such small pressure fluctuations are difficult to measure. This term mainly redistributes TKE but it can also move energy out of the BL, e.g, in the presence of gravity waves (Stull, 1991).



### 1.2.4 Winds in the PBL

Due to the influence of the surface friction and therefore the influence of roughness, a logarithmic wind profile forms that is dependent on the atmospheric conditions. To describe the wind profile in a mathematical way one can start from the Reynolds equations from section 1.2.2 by considering a zonal flow oriented in the x direction

$$\frac{\partial \bar{u}}{\partial t} = -\bar{u} \frac{\partial \bar{u}}{\partial x} - \bar{v} \frac{\partial \bar{u}}{\partial y} - \bar{w} \frac{\partial \bar{u}}{\partial z} - \frac{1}{\rho_0} \frac{\partial \bar{p}}{\partial x} + f\bar{v} + \nu \nabla^2 \bar{u} - \frac{\partial \overline{u'u'}}{\partial x} - \frac{\partial \overline{u'v'}}{\partial y} - \frac{\partial \overline{u'w'}}{\partial z}. \quad (1.25)$$

Moreover, a stationary flow with horizontally homogenous motion is assumed, as well as a balance between the horizontal pressure gradient and friction, due to the small impact of the Coriolis force in low altitudes compared to the other forces. Following these assumptions only one term of equation 1.13 remains.

$$\frac{\partial}{\partial z} \overline{w'u'} = 0 \quad \Rightarrow \quad \overline{w'u'} = \text{const}(\text{with height}) \quad (1.26)$$

Since this equation is non linear it needs to be parametrized in order to solve it. There are several ways to do that. One of them is the gradient formulation, where turbulent fluxes of a variable  $\chi$  with the wind component  $u_i$  are related and opposite to their gradient. Turbulence is working against the established gradient,

$$\overline{u'_i \chi'} \propto -\frac{\partial \bar{\chi}}{\partial x_i}. \quad (1.27)$$

The correct dimension of that relationship is established through the turbulent diffusion coefficient  $K_\xi$ , which can be parametrized through the introduction of Prandtl's mixing length  $l$  and the characteristic flow speed  $u_c$ . This is a measure of the ability of turbulence to cause mixing (Stull, 1991).

$$\overline{u'_i \xi'} = -K_\xi \frac{\partial \bar{\xi}}{\partial x_i} \quad (1.28)$$

$$K_\chi = -\overline{w'l'} = u_c l \quad (1.29)$$

If this parameterization is applied to equation 1.26 one gets the turbulent momentum flux

$$\overline{w'u'} = -K_m \frac{\partial \bar{u}}{\partial z}, \quad (1.30)$$

with  $K_m$  being its the diffusion coefficient. It is useful to re-write the turbulent flux in units of velocity, which is done with the so-called shear velocity  $u_*$  (Mayer, 2009). For the parameterization of the diffusion coefficient, the above mentioned characteristic flow speed  $u_c$  and mixing length  $l$  are used. The index in  $u'_0$  indicates ground near perturbation of the zonal wind speed.

$$u_* = \sqrt{-\overline{w'u'_0}} \quad \text{and} \quad u_c = l \frac{\partial \bar{u}}{\partial z} \quad (1.31)$$

If the case of a neutral stratification is considered, one can define the mixing length as the height multiplied by the Kármán constant  $\kappa$ , which is retrieved experimentally and equals 0.4

$$l = \kappa z. \quad (1.32)$$

The insertion of equations 1.31 and 1.32 into equation 1.30 and its rearrangement in terms of the vertical gradient of horizontal velocity leads to

$$-u_*^2 = -u_c l \frac{\partial \bar{u}}{\partial z} \quad \Rightarrow \quad u_*^2 = \kappa z \frac{\partial \bar{u}}{\partial z} \kappa z \frac{\partial \bar{u}}{\partial z} \quad (1.33)$$

$$\Rightarrow \quad \frac{\partial \bar{u}}{\partial z} = \frac{u_*}{\kappa z}. \quad (1.34)$$

Integrating equation 1.34 from the ground  $z_0$  to the height  $z$  is the final step for the equation of the mean wind speed as a function of the height for neutral atmospheric conditions

$$\bar{u}(z) = \frac{u_*}{\kappa} \log\left(\frac{z}{z_0}\right). \quad (1.35)$$

For a stable and unstable case, a stability-dependent function  $\Psi$  is introduced, which is negative for stable and positive for unstable conditions (Tong, 2010).

$$\bar{u}(z) = \frac{u_*}{\kappa} [\log\left(\frac{z}{z_0}\right) - \Psi] \quad (1.36)$$

$\Psi$  is defined as

$$\Psi = \xi\left(\frac{z - z_0}{L}\right) \quad (1.37)$$

where  $L$  is the Monin-Obukhov length, which represents the heights of the layer in which the mechanically produced turbulent energy dominates over the thermally

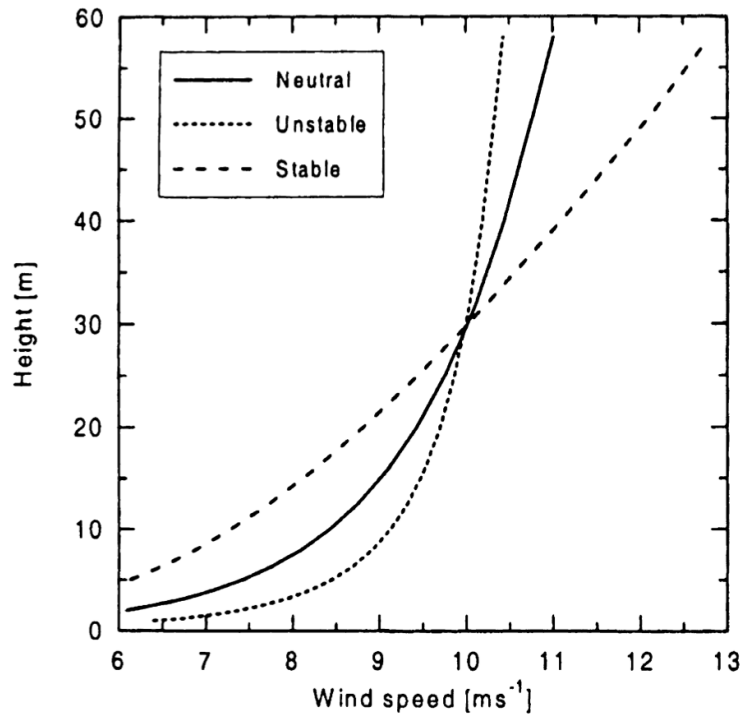


Figure 1.3: Logarithmic wind profiles dependent on atmospheric condition (Tong, 2010)

induced one.  $\xi$  is an experimental constant (in most of the cases  $\xi = 5$ ). The logarithmic wind profiles, described by equations 1.35 and 1.36, under different atmospheric conditions are illustrated in figure 1.3. (Mayer, 2009)

## 1.3 LIDAR

Light Detection and Ranging (LIDAR) is one of remote sensing techniques commonly used in boundary layer meteorology. Compared to in-situ measurements, remote sensing provides more extensive temporal and spatial data coverage, which makes the profiling of the atmosphere and the determination of highly variable atmospheric parameters possible. LIDAR instruments can be ground-based or airborne. However, their utility for the most part is limited to the occurrence of tracers, for example to the presence of aerosols, which is the case for the backscatter LIDARs

The history of the LIDAR principle is discussed by Weitkamp (2005) and dates back to pre-laser times, when, for example, in 1938 light pulses were used to measure cloud base heights for the first time. The rapid development of LIDAR started with the invention of laser in 1960. From then on was coherent with the further laser development.

### 1.3.1 LIDAR Setup

A LIDAR system basically consists of a transmitter and a receiver. A laser transmits short light pulses that are mostly expanded before sent into the atmosphere and a telescope that collects the backscattered photons. The received radiation is filtered by an optical analyzing unit, depending on the application, and is sent to a detector, where the information is converted into an electrical signal that is processed by a computer.

### 1.3.2 LIDAR Equation

The LIDAR equation describes the power of the received optical signal dependent on the technical settings and the conditions of the atmosphere, which is nicely evaluated by Weitkamp (2005).

The laser transmits pulses with the power of  $P_0$  into the atmosphere reaching a scattering volume at a distance  $R$ , where  $R_1$  is the distance between the leading edge

and the device, whereas  $R_2$  is the distance between the tailing edge and the device. These can be calculated as

$$R_1 = \frac{ct}{2}, \quad R_2 = \frac{c(t - \tau)}{2} \quad (1.38)$$

$$\Delta R = R_1 - R_2 = \frac{c\tau}{2}. \quad (1.39)$$

$\tau$  is the temporal pulse length,  $t$  is the time at which the signal is detected at the receiver and  $c$  the speed of light. If one looks only one way the factor  $\frac{1}{2}$  appears. The power density of the laser measured at a point in the atmosphere is given by

$$P_d = \frac{P_0}{A_L}, \quad (1.40)$$

where  $A_L$  is the laser beam cross section. If we now consider the laser pulse power at an area of points, namely at the scattering area one gets

$$P_S = P_0 \frac{A_S}{A_L}, \quad (1.41)$$

where  $A_S$  is the scattering cross section. The scattering volume  $V$  is just the same as the volume of the pulse itself as is shown in figure 1.4 and is given by

$$V = A_L \Delta R = A_L \frac{c\tau}{2} \quad \Rightarrow \quad A_L = V \frac{2}{c\tau}. \quad (1.42)$$

Therefore the scattering area is given by

$$A_S = N \sigma_{sca} V, \quad (1.43)$$

where  $N$  is the concentration of the scattering particles and  $\sigma_{sca}$  the scattering coefficient, which is dependent on the wavelength and the scattering angle. Both values together lead to the backscattering coefficient  $\beta$  which is defined as

$$\beta(R, \lambda) = \sum_j N_j(R) \frac{\partial \sigma_{j,sca}}{\partial \Omega}(\pi, \lambda), \quad (1.44)$$

where considering the concentration of backscattering particles  $N_j$  of the kind  $j$  and the derived backscattering cross section at the wavelength  $\lambda$ . If there is only isotropic scattering of one type of particles, equation 1.44 simplifies to

$$4\pi\beta = N\sigma_{sca}. \quad (1.45)$$

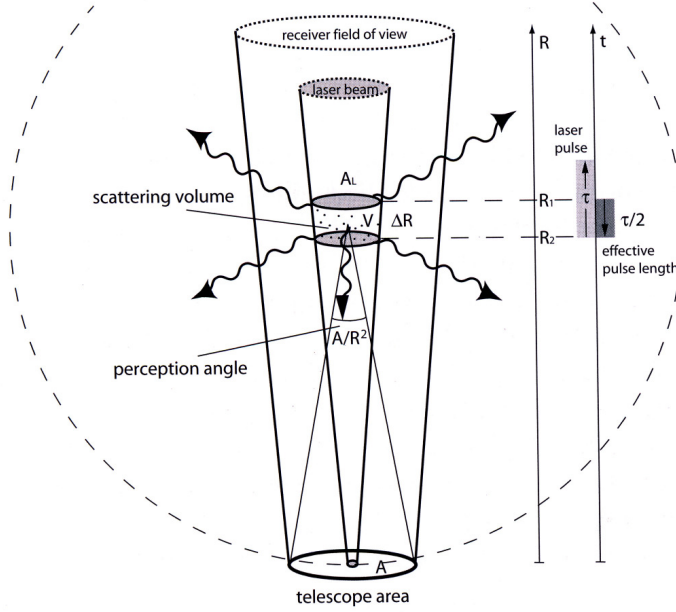


Figure 1.4: LIDAR geometry (Weitkamp, 2005)

Then the backscattered power from the particles is collected by the telescope and can basically be written as

$$P_C = P_S \frac{A_C}{4\pi R^2}, \quad (1.46)$$

where  $A_C$  is area of the collector. By inserting equation 1.41, 1.43, 1.42 and 1.45 into equation 1.46 one gets

$$P_C = P_0 \frac{A_S}{A_L} \frac{A_C}{4\pi R^2} = P_0 \frac{c\tau}{2} A_T \frac{1}{R^2} \beta. \quad (1.47)$$

For the final LIDAR equation we still need a few terms. One has to take into account the overall system efficiency  $\eta$  as well as the fact that the area of the telescope  $A_C$  is just a part of the area that encloses the backscattered volume. The latter is determined by the so-called laser beam receiver-field-of-view overlap function  $O(R)$ . One also has to consider that a part of the signal is transmitted into the atmosphere,

which can be quantified with the following transmission term  $T(R)$

$$T(R, \lambda) = \exp \left[ -2 \int_0^R \alpha(r, \lambda) dr \right], \quad (1.48)$$

where  $\alpha$  is the extinction coefficient. Taken the mentioned factors into account and rearranging eq. 1.47 one gets the final LIDAR equation

$$P(R, \lambda) = P_0 \frac{c\tau}{2} A\eta \frac{O(R)}{R^2} \beta(R, \lambda) \exp \left[ -2 \int_0^R \alpha(r, \lambda) dr \right]. \quad (1.49)$$

Equation 1.49 can be separated into four terms dependent on the LIDAR performance  $K$ , the measurement geometry  $G(R)$  and the atmospheric conditions in  $\beta(R, \lambda)$  and  $T(R, \lambda)$ .

$$P(R) = KG(R)\beta(R, \lambda)T(R, \lambda) \quad (1.50)$$

with

$$K = P_0 \frac{c\tau}{2} A\eta \quad \text{and} \quad G(R) = \frac{O(R)}{R^2} \quad (1.51)$$

### 1.3.3 LIDAR Techniques

Dependent on the research field and the area of interest, one can use different LIDAR types based on different measurement principles. These types are shortly described below and can be looked up in Weitkamp (2005) for more detail. The main focus is on the Doppler Wind LIDARs because the Leosphere WINDCUBE<sup>TM</sup> belongs to that category.

#### Elastic Backscatter LIDAR

The Elastic Backscatter LIDAR is the simplest type of LIDAR. The explanation of section 1.3.2 applies to this type of LIDAR. A single wavelength is transmitted into the atmosphere and elastically scattered back to the receiver, which means that the wavelength of the radiation remains unchanged. As the scatter intensity is dependent on the size of the particle compared to the wavelength, one can obtain information

about the presence and location of aerosol and cloud layers. Additionally, a non-spherical shape changes the polarization state of the transmitted radiation, which is useful for examining cirrus clouds and dust layers.

### **Differential Absorption LIDAR (DIAL)**

Using the Differential Absorption LIDAR technique, two different wavelengths are transmitted almost simultaneously (at an interval of less than a few nanoseconds). Considering that one wavelength is absorbed differently than another, a differential absorption coefficient can be determined that is also dependent on the molecule type. If this coefficient is known for the two wavelengths, the number concentration of the gas atoms or molecules can be derived. Therefore the main application of this technique is the detection of gases and their concentrations, such as water vapor ( $H_2O$  DIAL) or carbon dioxide ( $CO_2$  DIAL).

### **Raman LIDAR**

The Raman LIDAR technique got its name from Raman scattering which is inelastic. Inelastic scattering involves the change of energy state of the particle and thus its vibrational-rotational energy level. This leads to a frequency shift that is proportional to the energy difference of the scatterer which is dependent on the molecular type. Therefore, water vapor profiles can be determined. By measuring the intensity distribution of the backscattered radiation one can calculate the temperature of the scattered volume according to the Stefan-Boltzmann law, which leads to the determination of temperature profiles.

### **Fluorescence LIDAR**

Measuring components of the upper atmosphere is possible with the Fluorescence LIDAR because metallic atoms and ions are present. If the energy of the transmitted photon collides with the energy of transition in an atom, ion or molecule, its rise to another energy level is initiated. The atom starts to fluoresce and reemits radiation



with the same wavelength as the laser. Therefore the resonance scattered signal is strong in magnitude which makes the detection of small concentrations possible.

### Doppler LIDAR

The Doppler LIDAR technique is based on the Doppler shift in the frequency of the backscattered signal. This happens when the particle that scatters the radiation is moving away or towards the laser beam. The frequency of the scattered light is given by

$$f = f_0(1 + \frac{v}{c}), \quad (1.52)$$

where  $f_0$  is the frequency of the emitted light,  $v$  the relative speed of the scatterer and  $c$  the speed of light. Because the signal is scattered all the way back to the transmitter, the Doppler shift is applied on both ways

$$f = f_0 + f_0 \frac{v}{c} + f_0 \frac{v}{c} = f_0(1 + \frac{2v}{c}). \quad (1.53)$$

The speed of the particle along the line-of-sight of the laser beam can now be calculated by inverting the equation 1.53. This principle can be applied to all Doppler LIDAR measurements.

Considering Doppler Wind LIDARs one calculates the wind speed out of the Doppler shift of a signal sent into the atmosphere that is scattered back by aerosols that travel with the air motion. A positive Doppler shift corresponds to a motion towards the LIDAR and a positive line-of-sight velocity and vice versa. As one can see in 1.53 the frequency shift is proportional to the ratio between the speed of the particle, which is the radial wind speed, and the speed of light. As the speed of light is much faster than the wind speed of air masses, the signal difference can be very weak and hard to detect. There are two detection techniques in use that try to measure the Doppler shift as accurately as possible. Both are briefly described below.

### Direct Detection

Directe detection works with the original backscattered signal, which has to run through different filtering processes before it is detected. Because each photon car-

ries a random wavelength according to the aerosol or molecular spectrum (Werner, 2001) the signal is split up into two channels, the molecular and the aerosol channel, and is then measured from two detectors. The spectrum width is dependent on the prevailing temperature which makes the detection technique dependent on another variable. Before detection, the signal runs through high resolution aerosol and molecular interferometers. Corresponding to the wind speed the photon wavelength is shifted which is the final signal that is measured after the filtering processes.

### Heterodyne Detection

The heterodyne principle describes the generation of a new frequency through mixing two independent frequencies together. By doing so the sum of both individual frequencies and their difference is built, while only the difference is of importance because the sum is larger than the cutoff frequency of the detector. In fact the incoming backscattered signal is mixed with the radiation of a local oscillator and their frequency difference can be determined with great accuracy.

A coherent Doppler LIDAR therefore consists of the components pictured in figure 1.5. TE stands for the Transmitter, D1 is one of the heterodyne detectors where the local oscillator is mixed with the outgoing signal and at D2 with the Doppler-shifted backscattered signal. The local oscillator (LO) also is a laser that is connected to the pulsed laser transmitter with a locking loop (LL)(Weitkamp, 2005).

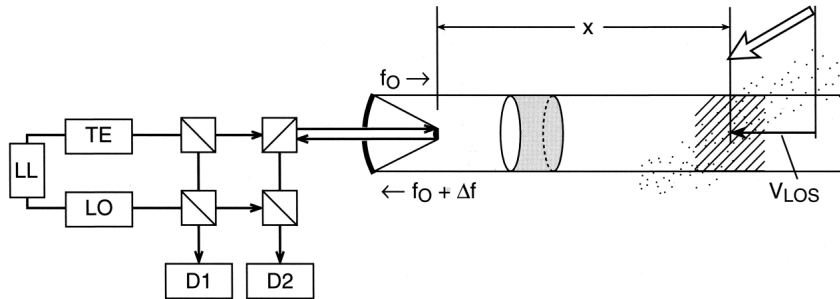


Figure 1.5: Principle of a heterodyne detection (Weitkamp, 2005)

---

### Continuous-Wave Doppler LIDAR

The transmitted radiation can either be in pulses or continuous. For a continuous-wave (cw) Doppler LIDAR a continuous, consistent emission of light along the laser beam axis is considered. It can only measure a single range at a time, dependent on the focus. The depth range  $\Delta x$  of the scattering volume is in direct relation to the distance  $x$  that is in focus and inversely proportional to the detector area  $A$ .

$$\Delta x = \frac{4x^2\lambda}{A}, \quad (1.54)$$

where  $\lambda$  is the transmitted wavelength. As the depth of the sampling volume increases with greater heights, the measurement is not representative anymore for the focused distance at high altitudes and therefore this technique is limited to the lowest parts of the atmosphere.

### Pulsed Doppler LIDAR

Compared to the cw LIDAR the Pulsed Doppler LIDAR can measure in multiple range gates simultaneously. Concerning the temporal resolution the pulsed LIDAR needs more time to collect the data because in addition to the sampling time it has to wait until the pulses are back from their scatterer. The measurement principle of this technique is already described in section 1.3.2.

### Scanning techniques

In addition to different detection and transmitter techniques, there are also different scanning techniques. Basically one can distinguish between two principles, the velocity-azimuth display (VAD) and the Doppler beam swing (DBS). In the VAD technique the LIDAR carries out a continuous conical scan with the cone-angle defined from the zenith to the direction the laser is looking at, which is adjusted by the instrument. The velocity is displayed as a function of the azimuth-angle  $\varphi$  as shown in the following equation. Hagen (2010) defines the elevation angle  $\theta$  as the angle

between the ground to the line-of-sight.

$$v_r(\varphi) = u \sin(\varphi) \cos(\theta) + v \cos(\varphi) \cos(\theta) + w \sin(\theta) \quad (1.55)$$

If the flow is homogenous and with little turbulence, only four measurements at azimuth-angle intervals of  $90^\circ$  are sufficient to calculate the wind vectors (Weitkamp, 2005). This is done in the DBS technique by applying equation 1.55 on 4 measurement points and is discussed below for the measurement principle of the WINDCUBE<sup>TM</sup> Doppler LIDAR.

# Chapter 2

## Methods and Data

### 2.1 WINDCUBE<sup>TM</sup>

WINDCUBE<sup>TM</sup> is a ground-based, active remote sensor that uses Laser Detection and Ranging technique in order to get three-dimensional wind profiles. The instrument is manufactured by LEOSPHERE in France. The main applications of the device can be found in the fields of wind energy and meteorology but also in air traffic in the context of turbulence analysis and air quality measurements (LEOSPHERE, 2008).

#### 2.1.1 Measurement Principle

The WINDCUBE<sup>TM</sup> makes use of the heterodyne Doppler Lidar measurement principle described in the previous section. Laser pulses are transmitted into the atmosphere into four different directions. Due to aerosols, dust and water drops the light is scattered back to the receiver of the device. If these particles move with the wind, the backscattered signal is shifted into a frequency different to that of the transmitter. The received optical signal is digitalized and sent to a computer to determine the scattered signal Doppler shift which is proportional to the velocity of the scattered target along the propagation path of the laser beam.

To make the detection easier the heterodyne principle described in section 1.3.3 is used. If the Doppler shift is known one calculates the radial wind speed along the line-of-sight and retrieves in that way the three-dimensional wind components. The

calculated wind field corresponds to the average of a 26 m thick layer of the atmosphere centered on the user defined altitude as one can see in fig. 2.1.

If more than one laser pulse is sent into the atmosphere with the known repetition

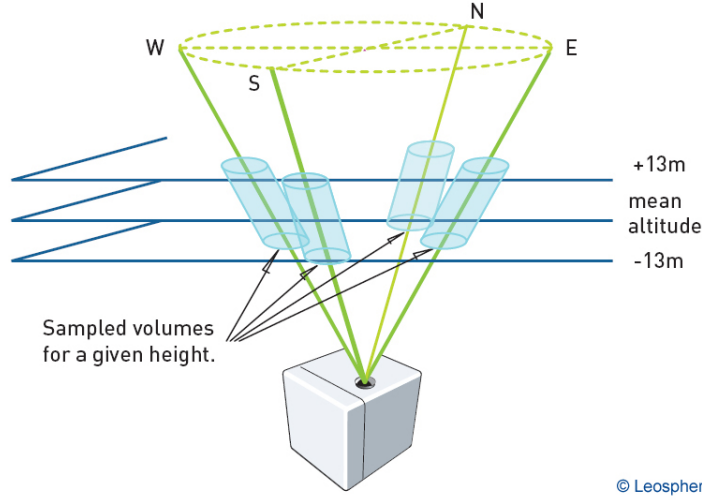


Figure 2.1: WINDCUBE<sup>TM</sup> sample volume (LEOSPHERE, 2008)

frequency and the length of the sample volume one gains information of up to ten different altitudes at one scanned line-of-sight from the time interval between the transmitted and the received signal.

### 2.1.2 Performance

Out of the given pulse length of 20 m and the number of shots with a repetition frequency of 20 kHz it is possible to calculate the data accumulation time  $t_1$ . This is done for 10 000 shots using the following equation

$$t_1 = 10^4 * 2 * 10^4 \text{ Hz} = 10^4 * \frac{1}{2} * 10^{-4} \text{ s} = 0.5 \text{ sec} . \quad (2.1)$$

Rotating the laser to the next position takes 0.5 seconds ( $t_2$ ), which leads us to data output frequency  $f$  of 1 Hz for one position or 4 Hz for every single position.

$$t_2 = 0.5 \text{ sec} \quad (2.2)$$

$$f = \frac{1}{t_1} + \frac{1}{t_2} = 1 \text{ Hz} \quad (2.3)$$

Minimum and maximum range of the device are dependent on the pulse length. Considering a 20 m long pulse the minimum range has to be 40 m to make sure that the transmitted signal has completely left the device and only the received signal is measured. In comparison to the minimum, the maximum range is mainly dependent on the power of the laser and the weather conditions.

Since the wavelength of  $1.5 \mu\text{m}$  of the laser is not in the visible range, there is no danger for the eye (eye-safe) and almost no radiation is absorbed by the atmosphere, as shown in figure 2.2.

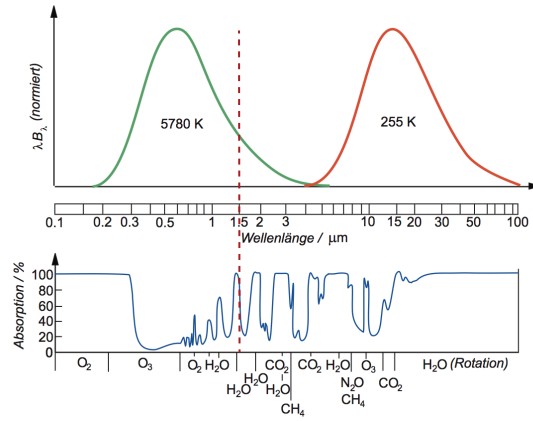


Figure 2.2: Relative absorption of radiation by the atmosphere as a function of the wavelength. The dashed line indicates the wavelength of the WINDCUBE™ laser. (Mayer, 2009)

The most important performance characteristics of the WINDCUBE™ Doppler LIDAR are summarized in tab. 2.1 below.

Performances	
Range	40 to 200 m
Data output frequency	4 s per position
Positions	4
Measurement levels	10
Sample length	20 m
Scanning cone angle	30°
Wind speed range	0 to 60 m/s
Wind speed accuracy	0.2 m/s
Wind direction accuracy	1.5°
Laser	
Wavelength	1543 nm
Pulse energy	10 $\mu J$
Pulse duration	200 ns
Repetition rate	20 kHz

Table 2.1: WINDCUBE<sup>TM</sup> characteristics (Aussibal, 2008)

### 2.1.3 Data Structure

Data is stored in two different files in ASCII format, one file with the raw data and the other one with a turbulence processed dataset using a ten-minute averaging period. Each day four data files were automatically generated, so two of each datasets per day are available for further evaluation.

The turbulence processed dataset consists of several parameters and their standard deviation are computed and listed. The parameters and their structure are summarized in table 2.2 concerning the raw data and in table 2.3 respective the turbulence processed data set. An important parameter is the Carrier-to-Noise-Ratio (CNR), because due to its value data is stored or disregarded, which will be discussed in the following section.

Examples of the data files can be found in the appendix.



File structure output raw data	
Data timestamp	dd/mm/yyyy hh:mm:ssss
Beam angular position	°
Temperature of the device	°C
Wiper	on/off
Data relative to the altitude	
Carrier to Noise Ratio (CNR)	dB
Radial wind speed	m/s
Averaged Doppler Spectrum width	m/s
Horizontal wind speed	m/s
Wind direction	°
Wind components u, v, w	m/s

Table 2.2: WINDCUBE<sup>TM</sup> file structure raw data (Aussibal, 2008)

File structure output turbulence processed data	
Data timestamp	dd/mm/yyyy hh:mm:ss
Wiper	Wiper count
Temperature of the device	°C
Data relative to the altitude	
10 min average + variance of horizontal wind speed	m/s
Maximal horizontal wind speed during past 10 min	m/s
Minimal horizontal wind speed during past 10 min	m/s
10 min averaged wind direction	°
10 min averages + variance of wind components u,v,w	m/s
10 min average + variance of CNR	dB
Maximal horizontal CNR during past 10 min	dB
Minimal horizontal CNR during past 10 min	dB
10 min average + variance of spectral broadening	m/s
Raw data availability during past 10 min	%

Table 2.3: WINDCUBE<sup>TM</sup> file structure turbulence processed data (Aussibal, 2008)

### 2.1.4 Data Accuracy and Availability

The accuracy of the device with respect to wind speed and direction is high enough for turbulence calculations and is estimated by Leosphere with the following values in table 2.4.

Data accuracy	
speed accuracy	0.2 m/s
direction accuracy	1.5 °

Table 2.4: WINDCUBE<sup>TM</sup> data accuracy

This accuracy is not constant as it is dependent on the atmospheric conditions. Therefore, there is a certain threshold at which this accuracy is not valid anymore. This threshold is constituted by a CNR smaller than -20 dB. If it falls below this value there is no calculation of the wind components, speed and direction. To indicate the data gap the value -999 is written into the data file. A visualization of this relationship between data gaps and a CNR smaller than -20 dB is shown in figure 2.4.

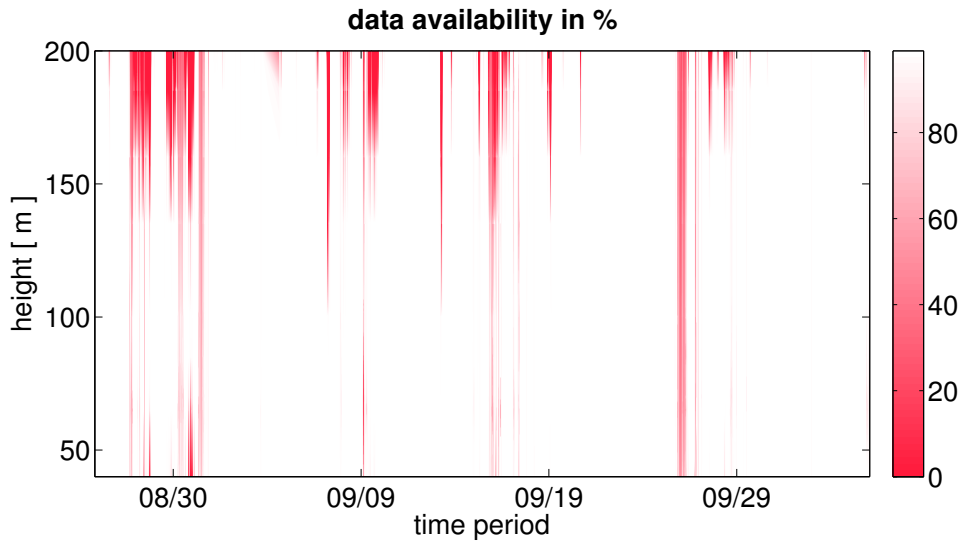


Figure 2.3: Availability of turbulence processed data in %

It is of interest to find the causes for a bad CNR to get a feeling for the limited use

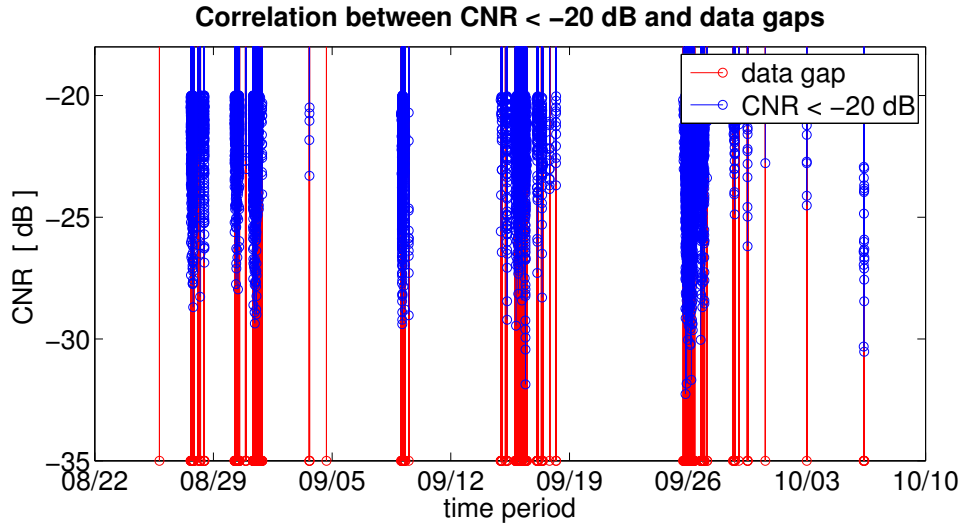


Figure 2.4: Correlation between data gaps and a CNR < -20dB

of the device. By recalling that the light pulses are scattered back by aerosols one recognizes that the data availability is dependent on the current weather conditions as the pulses could also be reflected by rain drops or cloud droplets. Figure 2.5 demonstrates that there is a clear interference of the CNR and the presence of rain, where the wiper activity of the device is correlated with the data availability.

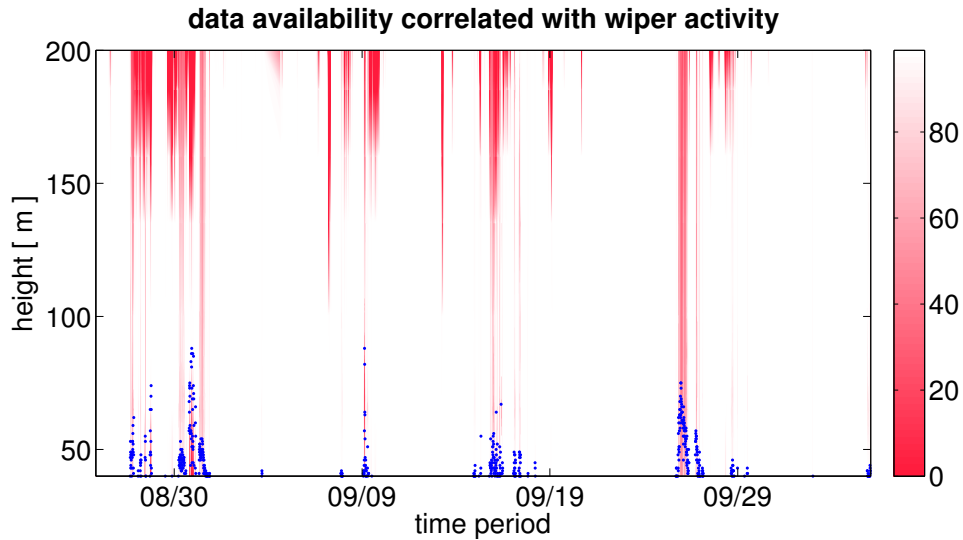


Figure 2.5: Correlation between data availability and wiper activity

The correlation between those factors is not perfect but it has to be considered that

there is no perfect correlation between wiper activity and the presence of rain. An example of September 7<sup>th</sup> at 06 UTC shows that the CNR is also sensible to low clouds that are pictured in the satellite image in figure 2.6. The slight yellow area indicates low clouds while the synop code of the weather station in Eisenstadt, which is located southwest of Bruck an der Leitha, reported fog at that time<sup>1</sup>. At the site data measured by the WINDCUBE<sup>TM</sup> is only available for the lower 100 m.

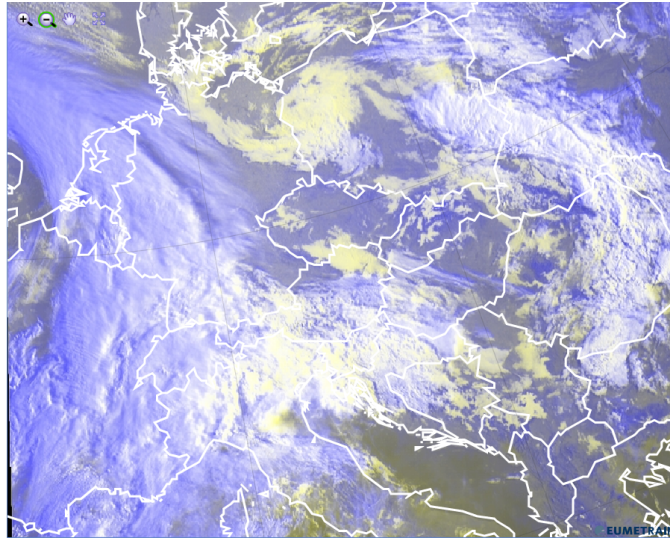


Figure 2.6: High resolution visible cloud image of September 7<sup>th</sup> at 06 UTC<sup>2</sup>

The accuracy is not the only limiting factor of the data availability but also technical problems of the device. As mentioned in section 2.3.2 the device had problems with its cooling system and therefore it did not produce a continuous time series. As most of the interest in the analysis is on the evolution of features as opposed to a single snapshot, the base of the analysis is a continuous time series. This is the reason for only using the data of the WINDCUBE<sup>TM</sup> WLS7-85.

<sup>1</sup>Source: [http://ogimet.com/display\\_synops.php?lugar=11035&tipo=ALL&ord=REV&nil=SI&fmt=html&ano=2010&mes=09&day=07&hora=00&anof=2010&mesf=09&dayf=08&horaf=12&enviar=Ver](http://ogimet.com/display_synops.php?lugar=11035&tipo=ALL&ord=REV&nil=SI&fmt=html&ano=2010&mes=09&day=07&hora=00&anof=2010&mesf=09&dayf=08&horaf=12&enviar=Ver), last accessed on February 7<sup>th</sup>, 2011

<sup>2</sup>Source: <http://www.eumetrain.org/eport/view.php?width=1920&height=1200&date=2010090706&region=euro>, last accessed on February 7<sup>th</sup>, 2011

## 2.2 Wind Vector Reconstruction

### 2.2.1 WINDCUBE<sup>TM</sup>

For reconstruction of the three-dimensional wind vector the WINDCUBE<sup>TM</sup> makes use of the DBS scanning technique described in the previous chapter. The WINDCUBE<sup>TM</sup> uses the following coordinate system in order to retrieve the wind vector. The pro-

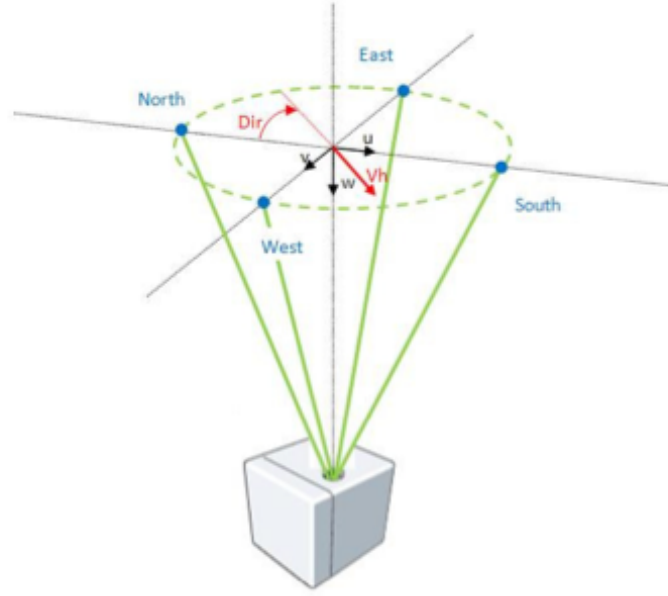


Figure 2.7: Orthogonal frame of the WINDCUBE<sup>TM</sup> for retrieving the wind components (LEOSPHERE, 2008)

jection of the wind vector (defined in figure 2.7) on the radial wind speed leads to

$$v_r(\varphi) = u \cos(\varphi) \sin(\theta) + v \sin(\varphi) \sin(\theta) + w \cos(\theta) \quad (2.4)$$

If measuring only at four different angles separated by  $90^\circ$  one gets a set of equations corresponding to the measurement points in North, East, South and West direction.

$$v_{rN} = u \sin(\theta) + w \cos(\theta) \quad (2.5)$$

$$v_{rE} = v \sin(\theta) + w \cos(\theta) \quad (2.6)$$

$$v_{rS} = -u \sin(\theta) + w \cos(\theta) \quad (2.7)$$

$$v_{rW} = -v \sin(\theta) + w \cos(\theta), \quad (2.8)$$

## 2.2. WIND VECTOR RECONSTRUCTION

where  $\theta$  is the cone angle and  $u, v, w$  are the three dimensional wind components. Solving the equations for  $u, v$  and  $w$  leads to

$$u = \frac{v_{rN} - v_{rS}}{2\cos(\theta)} \quad (2.9)$$

$$v = \frac{v_{rE} - v_{rW}}{2\cos(\theta)} \quad (2.10)$$

$$w = \frac{v_{rN} + v_{rE} + v_{rS} + v_{rW}}{4\sin(\theta)}. \quad (2.11)$$

Attention has to be paid to the definition of the retrieved wind vector with respect to the above mentioned coordinate system. Plotting the measured wind components calculated with the above equations at a specific time leads to a different orientation of the wind vectors with respect to the prevailing winds at that time, which is illustrated in figure 2.9

The reason of this false position of the wind vectors lies in the difference from the usual definition of the coordinate system in meteorology. The comparison of the two different coordinate systems is shown in figure 2.8.

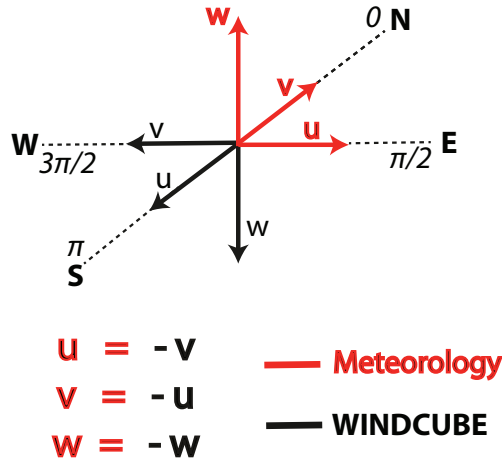


Figure 2.8: Comparison between the meteorological orthogonal frame and that of the WINDCUBE<sup>TM</sup>.

In terms of the calculations of wind speed and wind direction there is no difference between the two coordinate systems as one can see from the following equations.

$$v_h = \sqrt{u^2 + v^2} \quad (2.12)$$

## 2.2. WIND VECTOR RECONSTRUCTION

$$Dir = \underbrace{Modulo(360 + atan2(v, u), 360)}_{WINDCUBE} = \underbrace{Modulo(360 + atan2(u, v), 360)}_{Meteorology} \quad (2.13)$$

Concerning the interpretation of the data in chapter 3, a new coordinate system is introduced in section 2.2 to make a meteorological analysis possible.

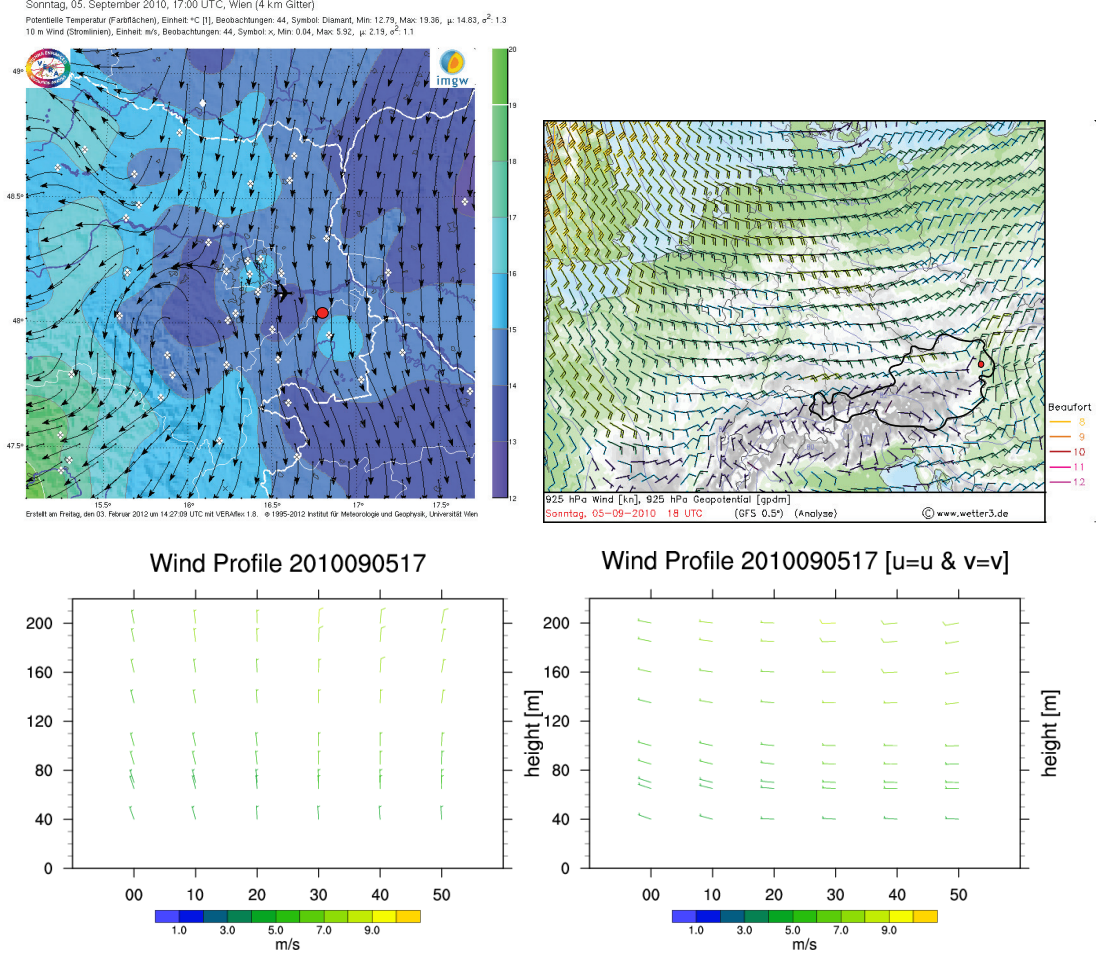


Figure 2.9: Bottom: 10 min vertical wind profiles of 17 UTC on September 5<sup>th</sup> for the meteorological coordinate system (left) and for the system of the WINDCUBE™ (right). Top: 10 m wind streamlines calculated with the analysis tool VERA at 17 UTC and wind barbs at 925 hPa calculated with the GFS analysis at 18 UTC

### 2.2.2 New Meteorological Reconstruction

For a correct meteorological analysis a new coordinate system needs to be defined to conform with the meteorological standards.

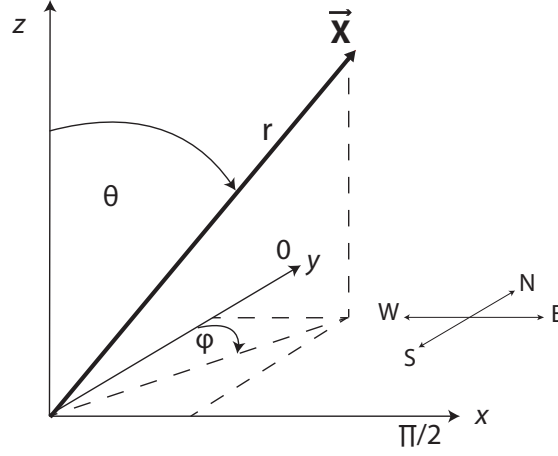


Figure 2.10: Orthogonal frame for retrieving the meteorologically defined wind components

Corresponding to that system, a vector  $\vec{X}$ , described by its spherical coordinates  $r$ ,  $\varphi$  and  $\theta$ , can be converted to its cartesian components  $x$ ,  $y$ ,  $z$  by

$$x = r \sin(\phi) \sin(\theta), \quad (2.14)$$

$$y = r \cos(\phi) \sin(\theta), \quad (2.15)$$

$$z = r \cos(\theta). \quad (2.16)$$

Thus, the first unit vector in the spherical system is defined as

$$\vec{e}_r = \frac{\vec{X}}{|\vec{X}|} = \vec{X} * \frac{1}{r} = \vec{e}_r = \begin{pmatrix} \sin(\varphi) \sin(\theta) \\ \cos(\varphi) \sin(\theta) \\ \cos(\theta) \end{pmatrix} \quad (2.17)$$

and describes the distance to the origin of the coordinate system.

Referring to the performance of the WINDCUBE<sup>TM</sup> it is important to look at the angles  $\phi$  and  $\theta$ , which are defined as  $[0, 2\pi[$  in clockwise direction and  $\theta = 27.37 = \text{const.}$  respectively. With the projection of the wind vector  $\vec{u} = (u, v, w)$  onto the radial component  $r$  of the vector  $\vec{X}$ , that is located in the line-of-sight, one gets an equation for the radial windspeed in dependence of the azimuth-angle and the local



## 2.2. WIND VECTOR RECONSTRUCTION

wind speed. The radial component of the vector  $\vec{X}$  therefore is representative of the radial wind speed  $v_r$ , which is measured by the device.

$$r = v_r = \vec{u} * \vec{e}_r \quad (2.18)$$

$$v_r(\varphi, u, v, w) = u \sin(\varphi) \sin(\theta) + v \cos(\varphi) \sin(\theta) + w \cos(\theta) \quad (2.19)$$

As mentioned in section 2.2.1 a horizontal homogeneous flow is assumed, leading to calculations at 4 measurement points with an azimuth-angle of  $0^\circ$  corresponding to North,  $90^\circ$  to East,  $180^\circ$  to South and  $270^\circ$  to West, assuming the cone-angle  $\theta$  to be constant.

$$v_{rN} = v \sin(\theta) + w \cos(\theta) \quad (2.20)$$

$$v_{rE} = u \sin(\theta) + w \cos(\theta) \quad (2.21)$$

$$v_{rS} = -v \sin(\theta) + w \cos(\theta) \quad (2.22)$$

$$v_{rW} = -u \sin(\theta) + w \cos(\theta). \quad (2.23)$$

Solving the equations 2.20 - 2.23 for  $u$ ,  $v$ ,  $w$ , respectively, leads to the equations for the wind components, assuming that these components do not change their value at all 4 measurement points during one calculation. For the calculation of one wind vector in one direction additional information of the 3 last scanned points is required (Neumann, 2011).

$$u = \frac{v_{rE} - v_{rW}}{2 \cos(\theta)} \quad (2.24)$$

$$v = \frac{v_{rN} - v_{rS}}{2 \cos(\theta)} \quad (2.25)$$

$$w = \frac{v_{rN} + v_{rE} + v_{rS} + v_{rW}}{4 \sin(\theta)} \quad (2.26)$$

As mentioned above, a few assumptions have to be made to rectify these calculations. They are going to be of great importance in the interpretation of the measured data later on.

The first and the most important assumption for the later analysis is the horizontal homogeneity of the wind field over the scanned disc (Weitkamp, 2005). At least for

---

## 2.2. WIND VECTOR RECONSTRUCTION

the last 3 points there is not only homogeneity in space but also in time. Therefore the temporal variation of the wind field always has to be smaller than the ratio between the beam distance to the next point and the horizontal wind speed (Boquet, 2006-2011). Additionally, it is assumed that the wind field is also constant within the measurement volume.

Taking all these assumptions into account it is possible to calculate the three dimensional wind vector as well as derived values, such as the horizontal wind speed  $v_h$  and the wind direction  $Dir$  using  $u$  and  $v$  from equation 2.24 and 2.25.

$$v_h = \sqrt{u^2 + v^2} \tag{2.27}$$

$$Dir = atan2\left(\frac{u}{v}\right) * \frac{180}{\pi} \tag{2.28}$$

## 2.3 Measurement Campaign

VERBUND Renewable Power GmbH conducted a measurement campaign for the duration of three months to collect three-dimensional wind data with the Leosphere WINDCUBE<sup>TM</sup> at a wind park near Bruck an der Leitha in Lower Austria. Data was collected between July 7<sup>th</sup> and October 6<sup>th</sup> 2010, primarily to get information about the wind profile at the location over the given time period. But there are more specific aims for the project, ranging from the verification of wind forecast models over intercomparison of wind parameters measured with cup anemometers to turbulence analysis and the analysis of small scale weather characteristics depending on the large scale weather situation.

### 2.3.1 Location

The measurement campaign took place in Bruck an der Leitha located at the border between Lower Austria and Burgenland in the eastern lowlands of Austria.

Looking at the topography of Eastern Austria in fig. 2.11 the wind park is placed east of the Alps in the southeastern part of the Wiener Becken, indicated by the red dot. This specific location with regard to the Alps is a promising region of high

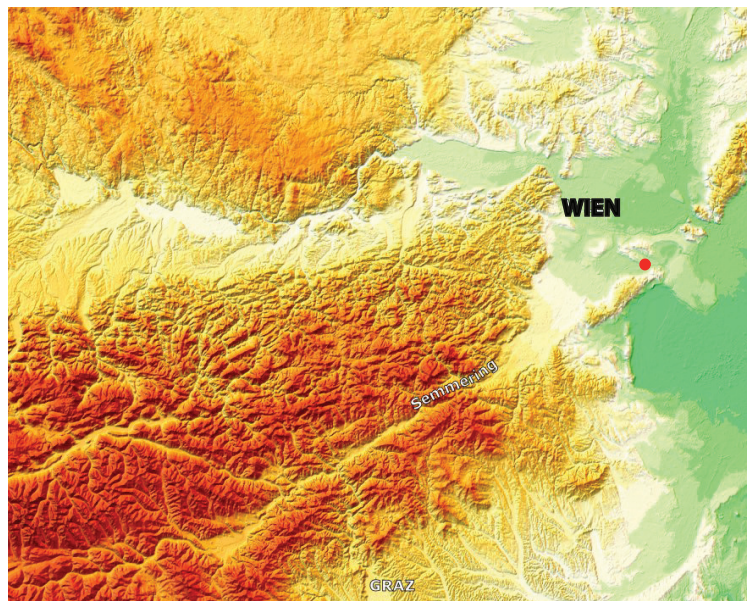


Figure 2.11: Topography of Eastern Austria<sup>3</sup>

### 2.3. MEASUREMENT CAMPAIGN

wind speeds due to the flow around the Alps. As will be seen later on, this location plays an important role in the interpretation of the collected data.

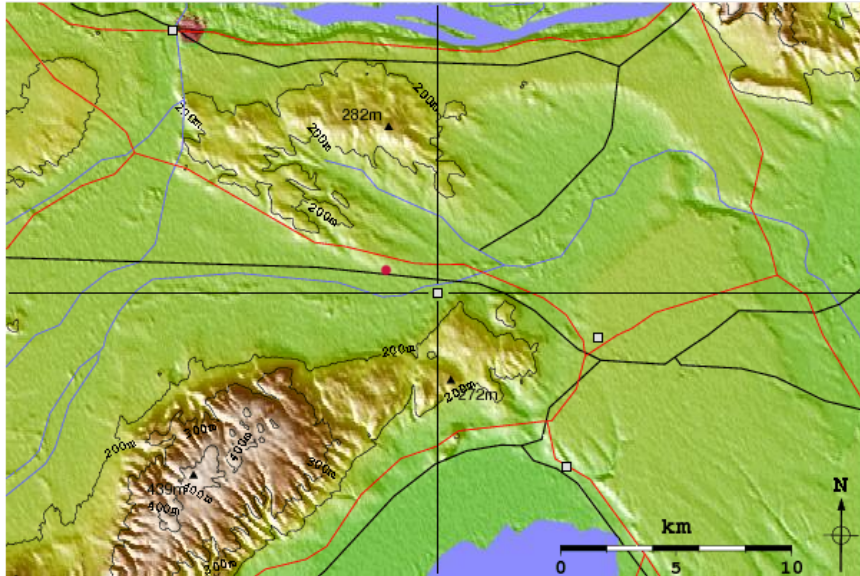


Figure 2.12: Topography of Bruck and the surrounding area <sup>4</sup>

Zooming into the surrounding area of Bruck an der Leitha in figure 2.12, one notices two small scale mountain ridges. In between these two, the red dot indicates the location of the Doppler LIDAR WINDCUBE™, the wind measurement device rented for the campaign. The exact coordinates are given in table 2.5. The white square to

Location	Latitude	Longitude	height [m amsl]
Wind park Bruck an der Leitha	48°01'48.98"N	16°43'26.48"E	175

Table 2.5: Location of the WINDCUBE™ (Bourgeois, 2010)

the right of the red dot marks Bruck an der Leitha. One of the two ridges is elongated in the west to east direction and located north of the wind park. Its highest peak is 282 m ASL. The other one, called Leithagebirge, is twice as high with the highest peak of 484 m ASL and extends from southwest to northeast south of the wind park.

<sup>3</sup>Source: [http://www.boehmwanderkarten.de/themen/galerie/stol\\_512\\_mr\\_oesterreich\\_hf.jpg](http://www.boehmwanderkarten.de/themen/galerie/stol_512_mr_oesterreich_hf.jpg), last accessed on February 6<sup>th</sup>, 2012

<sup>4</sup>Source: <http://www.weather-forecast.com/locations/Bruck-an-der-Leitha>, last accessed on November 23<sup>rd</sup>, 2011

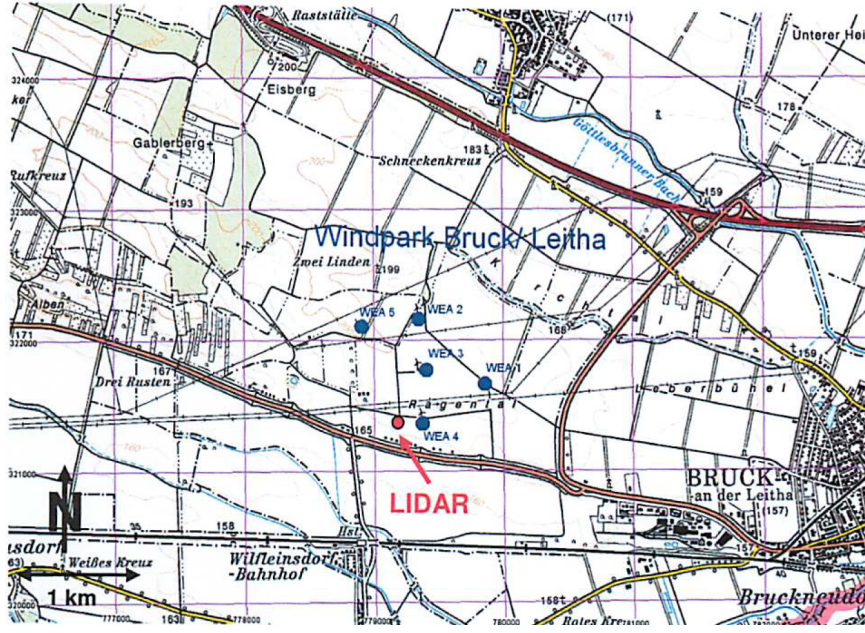


Figure 2.13: Wind park location (Bourgeois, 2010)

The wind park itself (fig. 2.13) is situated west of Bruck an der Leitha and consists of five wind turbines of the type Enercon E66 with a nominal power of 1.8 MW and a hub height of 65 m (Bourgeois, 2010).

### 2.3.2 Time Period and Setup

As mentioned before data was collected over a period of three months starting on July 7<sup>th</sup> and on October 6<sup>th</sup>, 2010. Due to a problem with the cooling system of the device, the WINDCUBE<sup>TM</sup> WLS7-70 did not collect data properly when it was overheated and therefore was replaced by a new one, the WLS7-85 on August 25<sup>th</sup>, 2010. For that reason only data from the WINDCUBE<sup>TM</sup> WLS7-85 is taken into account for the analysis from that day on. From September 3<sup>rd</sup> at 19 UTC to September 4<sup>th</sup> at 18 UTC there is a discontinuation of the measurement due to farmers work on the field where the WINDCUBE<sup>TM</sup> was located.

The WINDCUBE<sup>TM</sup> was placed 165 m west of the WEA<sup>5</sup> 4, on agricultural land. That distance is equivalent to 2.5 rotor diameters. With that distance the device is

<sup>5</sup>WEA stands for wind energy plant ("WindEnergieAnlage")

placed inside the wake area of the wind turbine as the minimum distance between two turbines in the main wind direction should be more than 5 rotor diameter (Tong, 2010).

As the WINDCUBE<sup>TM</sup> can measure at ten user defined altitudes at a time, ranging from a minimum height of 40 m up to a maximum of 200 m, there are nine different levels defined in the measurement campaign from VERBUND Renewable Power GmbH.

Level	Height above ground [ m ]
1	40
2	65
3	70
4	85
5	100
6	135
7	160
8	185
9	200

Table 2.6: WINDCUBE<sup>TM</sup> measurement altitudes

## 2.4 TKE Calculation

In the derivation of TKE in section 1.2.2 the Reynolds-average was introduced. In order to find out if 10 min is an appropriate averaging period the energy spectrum of the horizontal wind speed of the analyzed period is calculated and plotted in figure 2.15.

There is no regularly recurring process visible in the energy spectrum that would be disregarded with an averaging period of 10 min. Therefore we conclude that the Reynolds-averaging period of 10 min is a good choice for the calculation of the TKE. Regarding the calculations of vertical gradients of the wind components, which are necessary in order to retrieve the profile of TKE budget terms, the data has to be interpolated vertically because of the irregular spacing of different measurement altitudes. A vertical polynomial fit of the eighth degree is used to obtain data at the

vertical spacing of one meter.

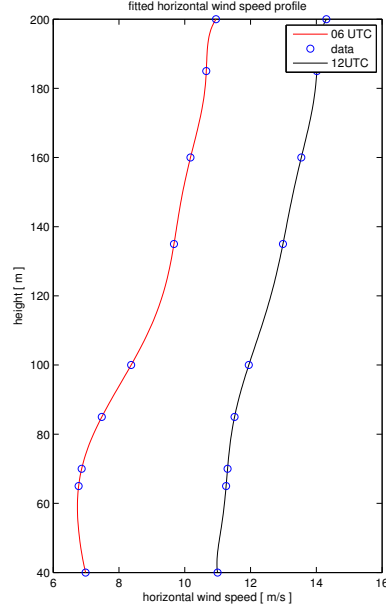


Figure 2.14: Polynomial fit of the horizontal wind speed at 06 and 12 UTC October 4<sup>th</sup>, 2010.

This makes the calculation of vertical gradients possible at a 5 m vertical resolution. Thus, the vertical advection, the vertical shear generation and the tendency of TKE can be calculated. This is not possible for horizontal gradients because horizontal homogeneity is assumed in the reconstruction of the wind vector.



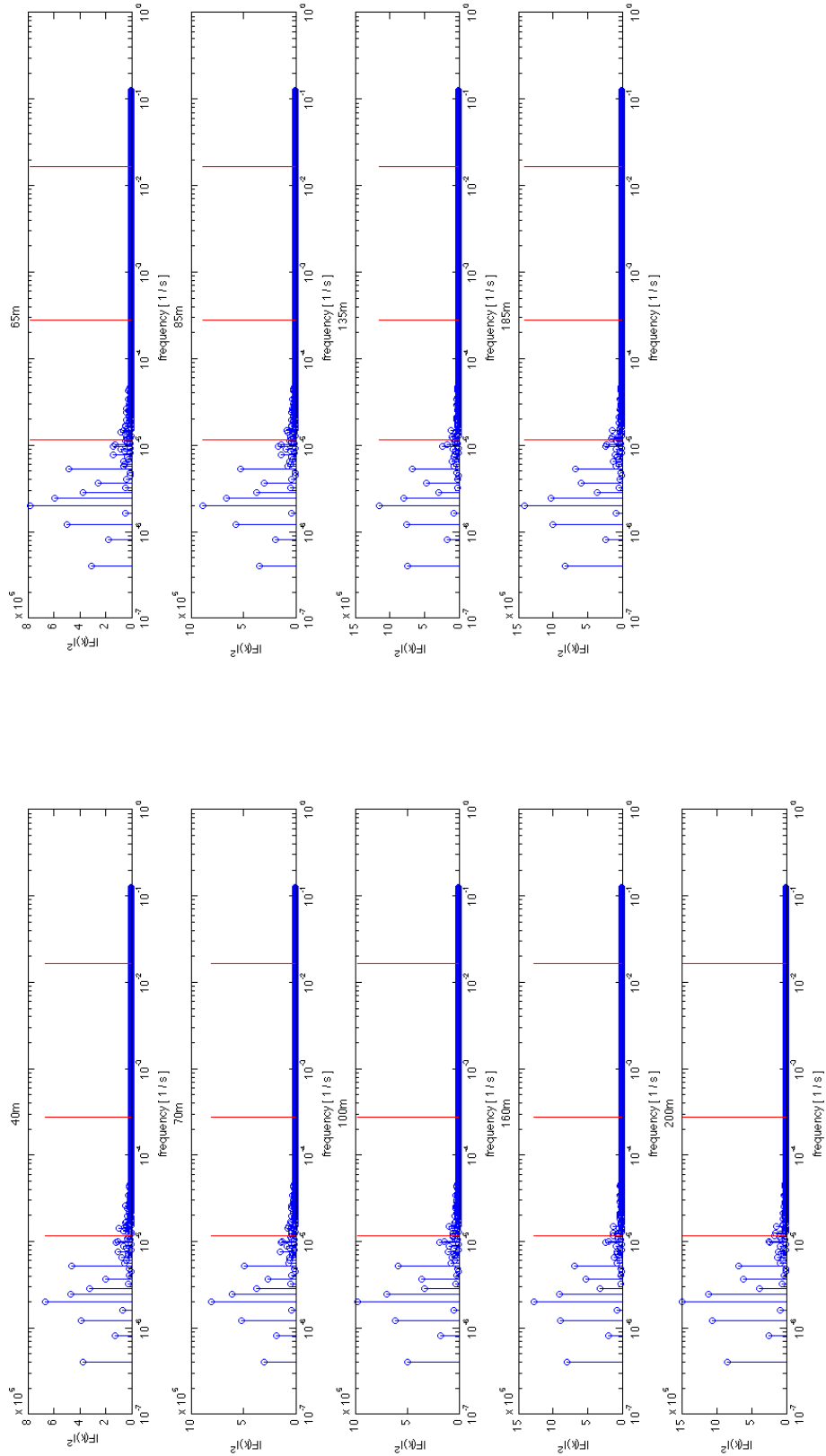


Figure 2.15: Energy spectrum of the horizontal wind speed calculated for each measurement height. The red lines indicate the frequency of a day, a hour and a minute respectively.



# Chapter 3

## Results and Discussion

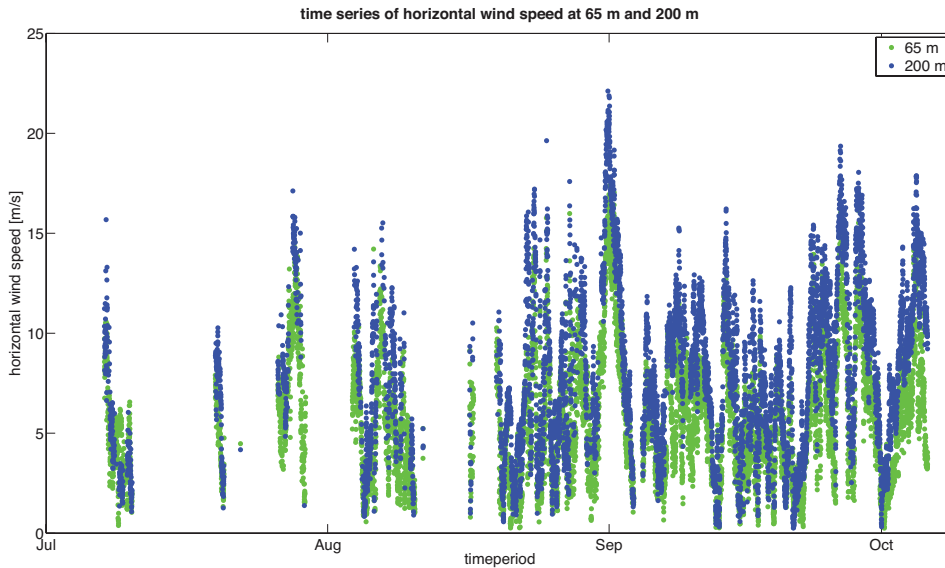


Figure 3.1: Total time series of the horizontal wind speed at 65 m (green line) and 200 m (blue line) measured by the WINDCUBES WLS7-70 and WLS7-85

Figure 3.1, in which horizontal wind speed is plotted against time, provides a nice outline of the turbulence processed dataset. In the time frame from July to the middle of August, the time series shows many temporal discontinuities. Due to an overheating problem of the device, explained in section 2.3.2, the data was lost. The increase in wind speed with height is visible in figure 3.1 from the difference in wind speed at two measuring heights. Furthermore the figure nicely illustrates the variable nature of wind speed over time. The wind speed is strongly dependent on the complexity of the terrain as well as on the prevailing weather conditions.

### 3.1 Observed Frequency of Wind Directions

The influence of the complex terrain on wind speed becomes evident from the shape of the wind roses<sup>1</sup> at different measurement heights (figure 3.2). Figure 3.2 shows wind direction as a function of wind speed and frequency. There is a clear influence of the surrounding terrain, as certain wind directions are absent from the wind roses.

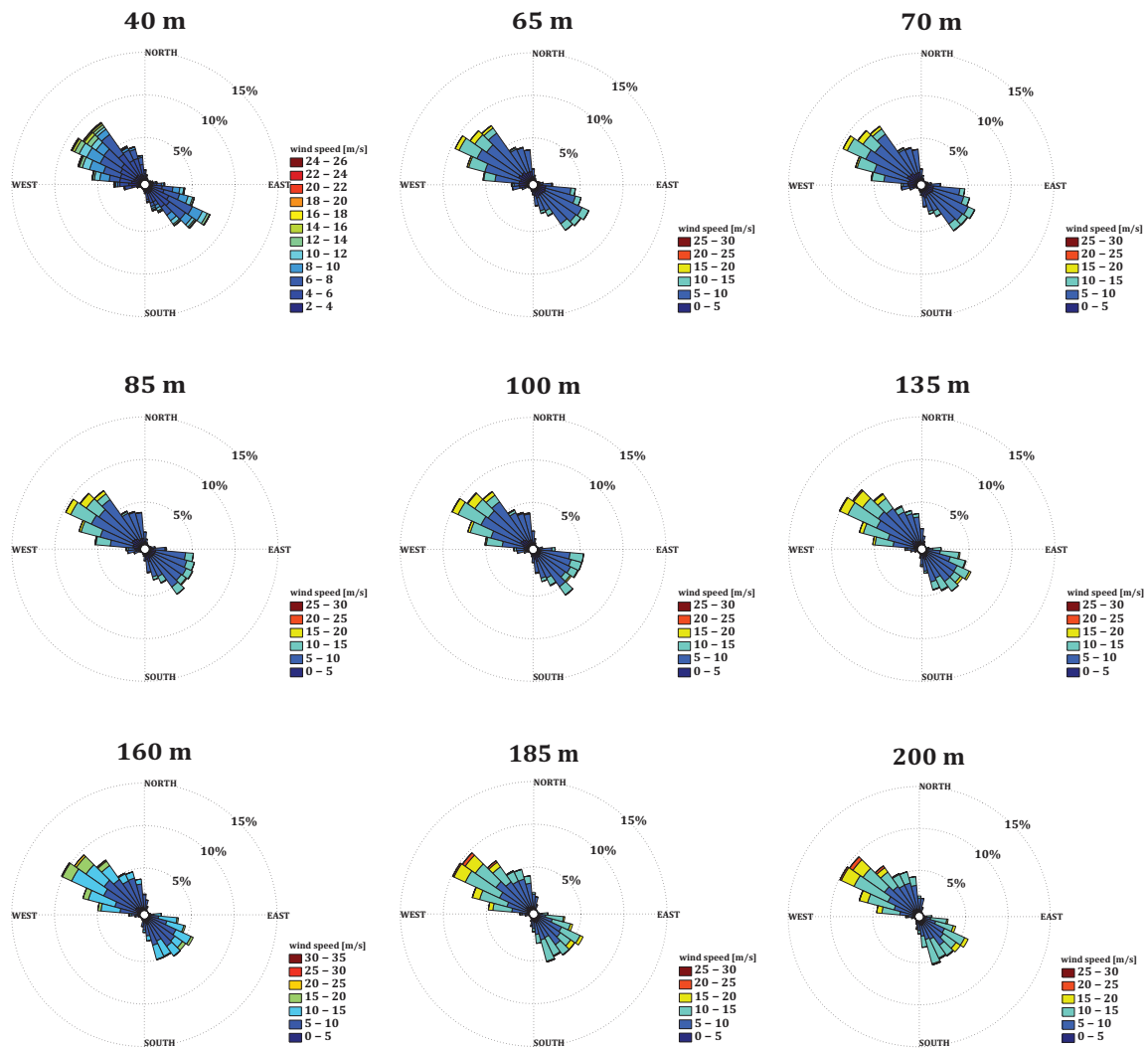


Figure 3.2: Wind roses from the Bruck an der Leitha wind park for the period of 26.8.2010-6.10.2010 with horizontal wind speeds greater than 3 m/s

<sup>1</sup>Code source: <http://www.mathworks.com/matlabcentral/fileexchange/17748-windrose>, last accessed on February 16<sup>th</sup>, 2012

### 3.1. OBSERVED FREQUENCY OF WIND DIRECTIONS

The small mountains located to the north and south of the measurement site channel the flow (figure 3.3). The additional large-scale influence of the Alps makes the northwest and southeast wind directions dominant. This phenomenon is rather well

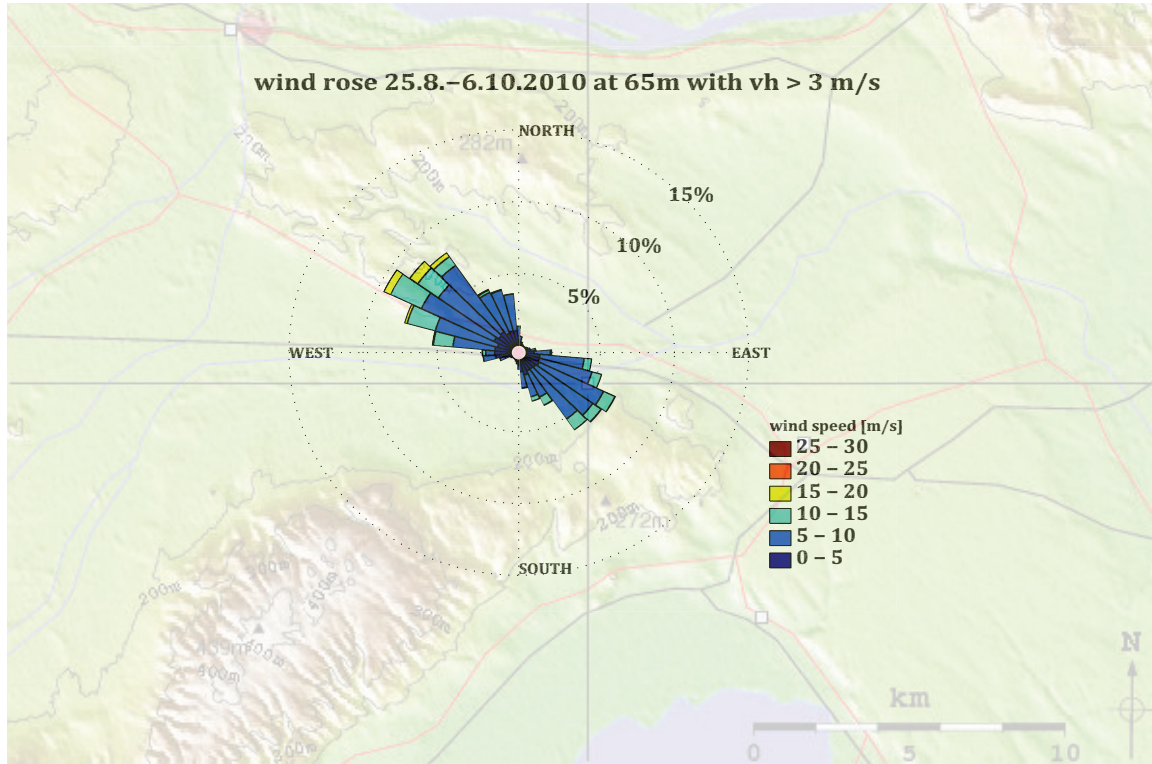


Figure 3.3: Wind rose at 65 m overlaid with the topography of the surrounding area

known and not limited to the measurement period alone (Lotteraner, 2009). In figure 3.4, the pattern can be recognized in the mean wind field over the Alps from 1980 until 2001.

At the site at Bruck an der Leitha, it is possible to utilize wind at speeds greater than  $3 \text{ m/s}$  for electricity generation via turbines. Hence, two different sets of wind direction frequencies at hub height were calculated, taking into account all wind speeds and only values great than the cut-in wind speed.

### 3.1. OBSERVED FREQUENCY OF WIND DIRECTIONS

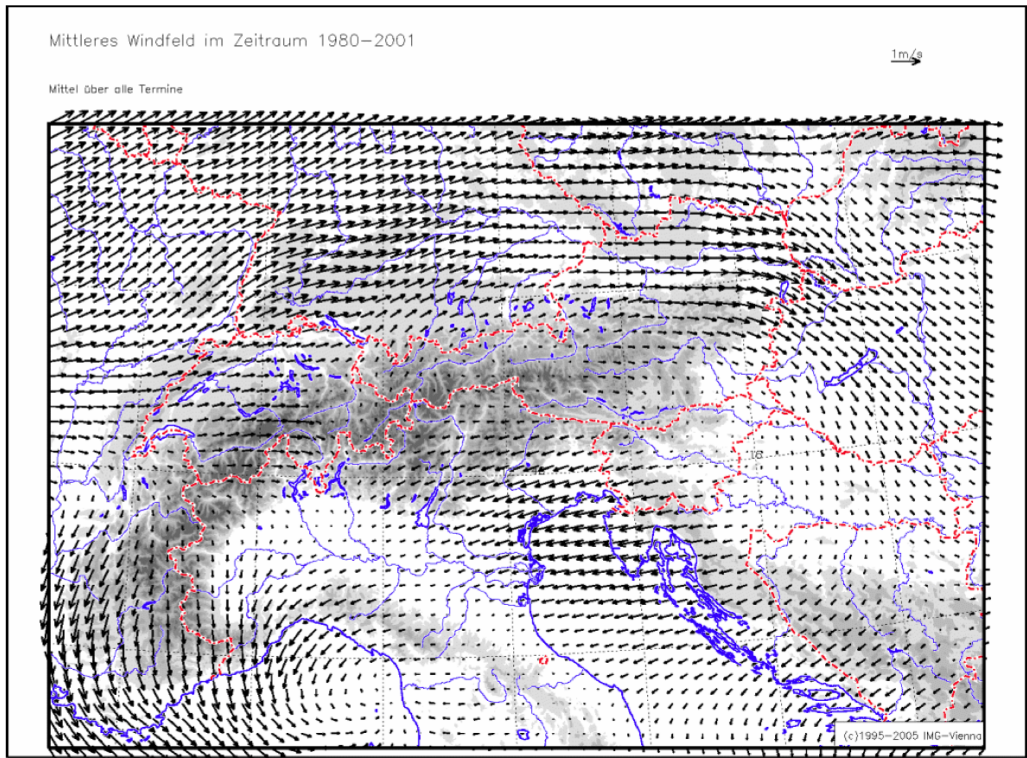


Figure 3.4: Mean wind field of the region of the Alps from 1980 until 2001 (Lotteraner, 2009)

Dir	%
NW	28,5
SO	23,4
W	16,3
O	12,9
N	7,9
S	6,6
NO	2,5
SW	1,9

Figure 3.5: Wind direction frequencies for all wind speeds.

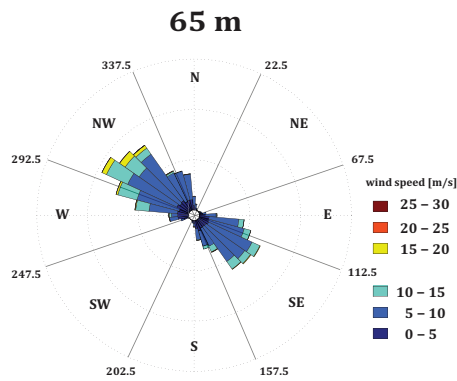


Figure 3.6: Wind rose at 65 m for wind speeds greater than 3 m/s

Dir	%
NW	24.3
SO	16.9
W	16,9
O	8.6
S	6.2
N	5.7
SW	1.4
NO	0.7

Figure 3.7: Wind direction frequencies for wind speeds greater than 3 m/s.

## 3.2 Weather classifications

As the terrain does not change with time, the relation between orography and the wind field was easily visualized. The influence of the prevailing weather situation on the wind field, however, is more complex and harder to discern. As winds are generated through pressure differences, it is necessary to consider pressure distributions at the surface, as well as geopotential distributions at higher altitudes to determine wind sources. The geopotential is the work that is necessary to lift an air parcel from the ground to a specific height. On the basis of these distribution patterns, predictions of the surface wind field or at the hub height can be made. These predictions are vital information for wind energy companies.

Computer models, such as the European Center for Medium-Range Weather Forecasts (ECMWF) model or the Global Forecast System (GFS), deliver general information on weather, hence, wind conditions, too, derived from the pressure and geopotential distributions. More detailed information can be obtained from higher resolution models, such as the Aire Limitee Adaptation dynamique Developpement International (ALADIN), which covers only the area of the Alps. To gather more information on how different weather conditions influence the wind field, weather classifications are used. Such classifications climatologically classify the weather situation of any given day over Europe, on the basis of pressure and geopotential distribution.

In this thesis the European Weather Pattern Catalog by Paul Heß and Helmut Brezowsky from Friedrich-Wilhelm Gerstengarbe (2005) is used, to classify the weather situations over the three months of the field campaign as well as for some statistics to see how frequent certain conditions are. The catalog distinguishes between 29 weather patterns listed in table 3.1.

Concentrating on the weather patterns during the given time frame of the measurement campaign one can classify that period as in table 3.2.

---

<sup>2</sup>Source: [http://www.dwd.de/bvbw/appmanager/bvbw/dwdwwwDesktop?\\_nfpb=true&\\_pageLabe=\\_dwdwww\\_spezielle\\_nutzer\\_hobbymeteorologen\\_klimainfos&T19607331211153463365254gsbDocumentPath=Navigation%2FOeffentlichkeit%2FWV%2FGWL%2F2010%2FSeptember%2FLuftmassen\\_\\_Node.html%3F\\_\\_nnn%3Dtrue](http://www.dwd.de/bvbw/appmanager/bvbw/dwdwwwDesktop?_nfpb=true&_pageLabe=_dwdwww_spezielle_nutzer_hobbymeteorologen_klimainfos&T19607331211153463365254gsbDocumentPath=Navigation%2FOeffentlichkeit%2FWV%2FGWL%2F2010%2FSeptember%2FLuftmassen__Node.html%3F__nnn%3Dtrue), last accessed on February 1<sup>st</sup>, 2012

Weather classes		
zonal circulation pattern		
1.	West condition, anticyclonic	WA
2.	West condition, cyclonic	WZ
3.	Southwest condition	WS
4.	Angular west condition	WW
mixed circulation pattern		
5.	Southwest condition, anticyclonic	SWA
6.	Southwest condition, cyclonic	SWZ
7.	Northwest condition, anticyclonic	NWA
8.	Northwest condition, cyclonic	NWZ
9.	Anticyclone Central Europe	HM
10.	Col Central Europe	BM
11.	Cyclone Central Europe	TM
meridional circulation pattern		
12.	North condition, anticyclonic	NA
13.	North condition, cyclonic	NZ
14.	Anticyclone Norwegian Sea-Island, anticyclonic	HNA
15.	Anticyclone Norwegian Sea-Island, cyclonic	HNZ
16.	Anticyclone British Isles	HB
17.	Trough Central Europe	TRM
18.	Northeast condition, anticyclonic	NEA
19.	Northeast condition, cyclonic	NEZ
20.	Anticyclone Fennoscandia, anticyclonic	HFA
21.	Anticyclone Fennoscandia, cyclonic	HFZ
22.	Anticyclone Norwegian Sea-Fennoscandia, anticyclonic	HNFA
23.	Anticyclone Norwegian Sea-Fennoscandia, cyclonic	HNFZ
24.	Southeast condition, anticyclonic	SEA
25.	Southeast condition, cyclonic	SEZ
26.	South condition, anticyclonic	SA
27.	South condition, cyclonic	SZ
28.	Cyclone British Isles	TB
29.	Trough West Europe	TRW
	Transition/undetermined	U

Table 3.1: Weather classes by Heß and Brezowsky

### 3.2. WEATHER CLASSIFICATIONS

Weather classes for the period of analysis									
August									
				26.	27.	28.	29.	30.	31.
				WZ	WZ	WZ	TRM	TRM	TRM
September									
1.	2.	3.	4.	5.	6.	7.	8.	9.	10.
TRM	NZ	NZ	NZ	HNFZ	HNFZ	HNFZ	HNFZ	HNFZ	TRM
11.	12.	13.	14.	15.	16.	17.	18.	19.	20.
TRM	TRM	TRM	TRM	WZ	WZ	WZ	BM	BM	BM
21.	22.	23.	24.	25.	26.	27.	28.	29.	30.
BM	BM	BM	U	TM	TM	TM	TM	HFZ	HFZ
October									
1.	2.	3.	4.	5.	6.				
HFZ	HFZ	HFZ	SA	SA	SA				

Table 3.2: Weather classes for the period of analysis by Heß and Brezowsky <sup>2</sup>

#### 3.2.1 Synoptic Weather Summary

In the beginning of the data collection period with the WINDCUBE<sup>TM</sup> WLS7-85, a zonal westerly flow over Central Europe allowed the fast passage of a few low pressure systems north of the Alps, leading to rainy weather in most parts of Austria and southwesterly to southeasterly winds in the East of Austria. The cyclogenesis and consequent cut-off from the basic flow over the Atlantic, added a northwest component to the surface wind field over Central Europe on August 28<sup>th</sup>. Therefore, cool, humid air was transported from the North to Austria resulting in unconventionally cold weather conditions for late August<sup>3</sup> with northwesterly winds. After the passage of another surface cyclone and the trough axis in the upper levels on August 31<sup>st</sup>, the cyclone in the east of Austria and the anticyclone over the British Isles generated a convergence zone. Therefore, a low-level jet over Eastern Austria with wind speeds over 15 m/s at a height of ten meters was established.

The expansion of the anticyclone from the British Isles to the Norwegian Sea and its small pressure gradient caused calm and sunny weather in Austria. At the same time, warm air advection on the east flank of the trough, now over eastern Europe, strengthened the old cyclone over Russia. Consequently, the cyclone propagated

retrograde to the Northwest. Austria remained in the influence of that cyclone, with northwesterly winds for most of the time, until September 7<sup>th</sup>. At that point, cold air advection in Western Europe lead to a development of new cyclones that were moving eastwards in the north of the Alps, leading to southeasterly winds in eastern Austria.

A weak westerly flow formed on September 10<sup>th</sup> that got replaced soon by a developing ridge over Central Europe, leading to its eastwards propagation. At the ground a col formed which is the reason for some sunny days in Austria. A new strong cyclone over the Norwegian Sea dominated the weather situation in Austria from September 15<sup>th</sup> onwards. The low pressure center north of Austria, lead to westerly winds.

A newly formed trough over the Atlantic, was amplified by a cold air outbreak on its way to Central Europe reaching the Mediterranean Sea. This lead to the formation of a Genoa cyclone that travelled with the basic flow northeastward similar to a Vb path. Consequently, easterly winds were prevailing in eastern Austria on September 25<sup>th</sup>. A new strong low pressure system from the Atlantic started to move eastwards, bringing, together with a high pressure system from Fennoscandia, warm air to the South of Central Europe. This created an amplifying ridge, with its axis over Austria on October 3<sup>rd</sup>. With the intense trough next to the ridge in the West, a strong southerly flow was established, leading to föhn North of the Alps until October 6<sup>th</sup>.

### 3.3 Case studies

The overview of the large scale weather conditions over Europe in the period of the measurement campaign, enables a more detailed analysis of the local weather conditions at the wind park. Utilizing general large-scale background information, small scale turbulence and flow characteristics can be analysed.

Dependent on the wind direction, as well as on the prevailing weather class and meteorological processes, four cases are selected for discussion. Each case covers a

---

<sup>3</sup>Reported by the Zentralanstalt für Meteorologie und Geodynamik (ZAMG), source: [http://www.zamg.ac.at/klima/klima\\_monat/wetterlagen?jahr=2010&monat=09](http://www.zamg.ac.at/klima/klima_monat/wetterlagen?jahr=2010&monat=09), last accessed on February 16<sup>th</sup>, 2012



time period of one day, starting from 00 MEZ (22 UTC of the previous day) until 00 MEZ of the next day (22 UTC of the previous day). The four cases contain two days where the weather situations is leading to the two main wind directions of the site, one convective day and one day during which the WINDCUBE<sup>TM</sup> was located downstream of the wind turbine.

For the analysis of the prevailing weather conditions, and to illustrate the meteorological parameters of that day, the GFS model<sup>4</sup> and the Vienna Enhanced Resolution Analysis (VERA) are used (Pötttschacher, 2000). The analyzing tool VERA takes the information of synoptic weather stations and interpolates these values to a regular grid. VERA has been developed at the University of Vienna and is optimized for the Alps domain (Tschannett, 2006). The GFS analysis corrects a first-guess model forecast with latest information from the global observation system (3D-Var). The GFS is a global model (NCEP) and therefore has a much lower resolution (27 km) compared to the VERA with a horizontal resolution of up to 1 km.

From the measured data 10 min averaged horizontal wind vectors are calculated and plotted in hourly time steps. Small wind barbs correspond to  $5m/s$ , whereas the large barbs correspond to  $10m/s$ .

---

<sup>4</sup>For information visite: <http://www.nco.ncep.noaa.gov/pmb/products/gfs/>, last accessed on February 16<sup>th</sup>, 2012

### 3.3.1 Northwesterly (NW) Case

The NW case deals with the situation on September 1<sup>st</sup>, when a low-level jet was present. As mentioned, the jet forms through a convergence zone of a high pressure system over the North Sea and a low pressure system over the Ukraine (figure 3.8). The jet is embedded in the trough over Central Europe, corresponding to the weather class TRM.

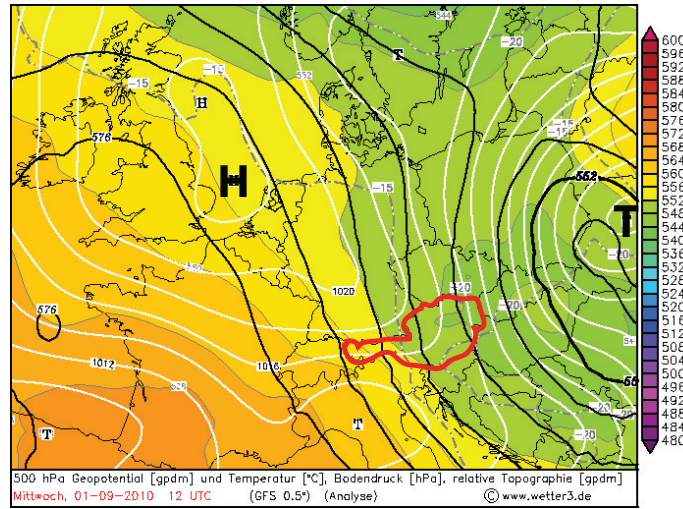


Figure 3.8: Surface pressure and 500hPa geopotential distribution over Central Europe from GFS at 12 UTC September 1<sup>st</sup>, 2010.

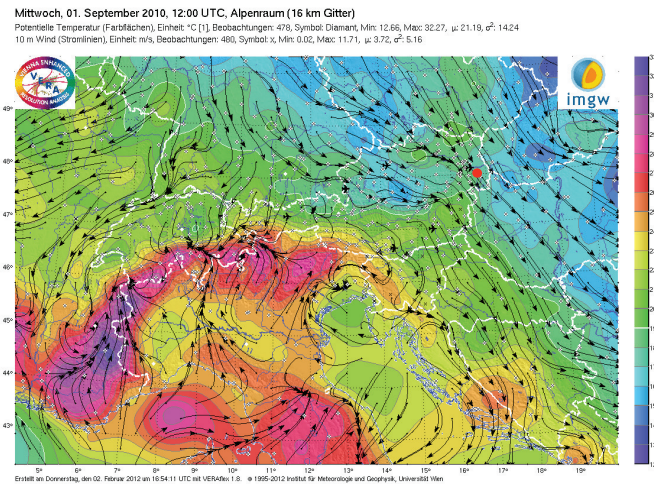


Figure 3.9: Streamlines of 10 m wind and potential temperature from VERA at 12 UTC September 1<sup>st</sup>, 2010.

The low-level jet is the dominant weather factor and the reason for northwesterly

winds with high speeds, ranging from 12 m/s at 40 m up to 20 m/s at 200 m, as one can see in figure 3.11. Because the jet shifts only slowly to the East, the wind direction is nearly constant over the whole day.

As seen in figure 3.11, the wind speed decrease with height as a result of friction

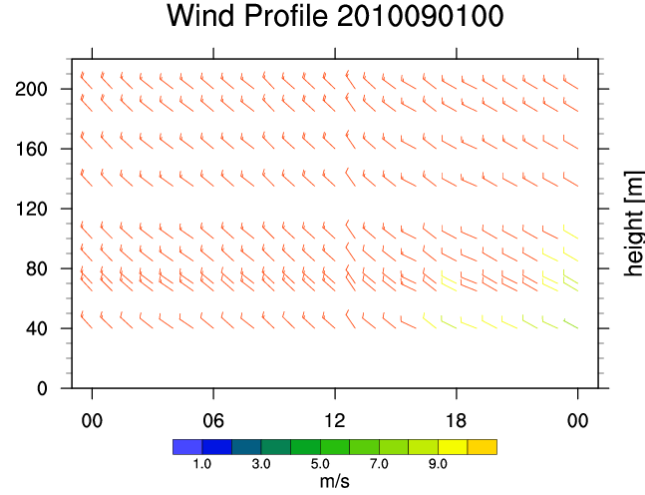


Figure 3.10: vertical wind profile (right) on September 1<sup>st</sup>

drag near the ground. Therefore high wind shear is persistent throughout the whole observed layer, leading to area-wide mechanical turbulence generation. Because of the high wind speeds and the resulting amount of high kinetic energy, TKE is, also relatively high. The maximum values of TKE during this period was around  $8 \text{ m}^2/\text{s}^2$ .

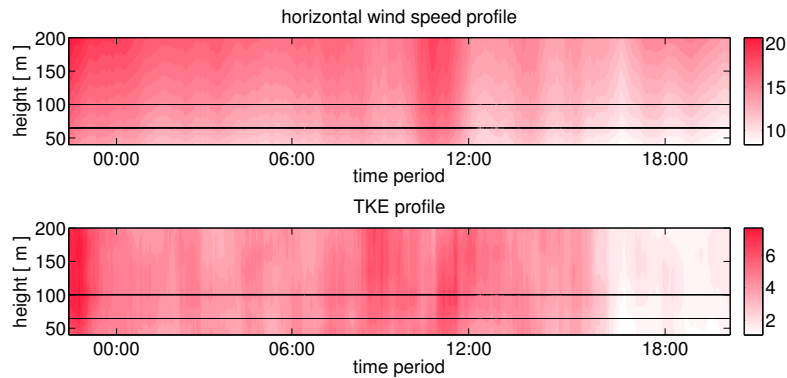


Figure 3.11: Vertical profiles of horizontal wind speed [m/s] and TKE [ $\text{m}^2\text{s}^{-2}$ ] on September 1<sup>st</sup>, 2010.

A snapshot at 12 UTC of the profiles of shear generation  $S$ , vertical advection  $AD$

and TKE tendency  $T$ , reveals a constant shear generation in a layer from 60 m to 190 m (figure 3.12).

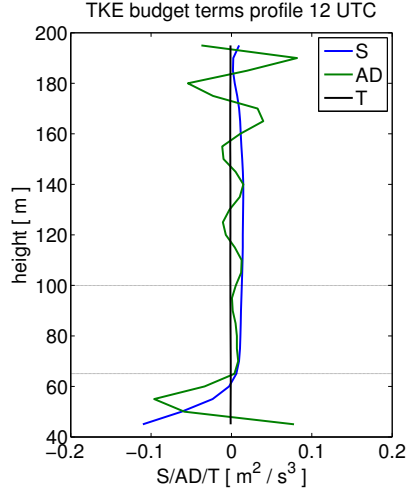


Figure 3.12: Profile of shear generation, vertical advection and tendency of the TKE budget on September 1<sup>st</sup> at 12 UTC.

### 3.3.2 Easterly (E) Case

A highly amplified trough west of Austria is the basis for interpretation of the weather situation on September 25<sup>th</sup>. A low with one closed isohyps, embedded within the trough over Central Europe, is the indicator of the weather class TM.

The large amplitude trough brings polar cold air into the region of the Mediter-

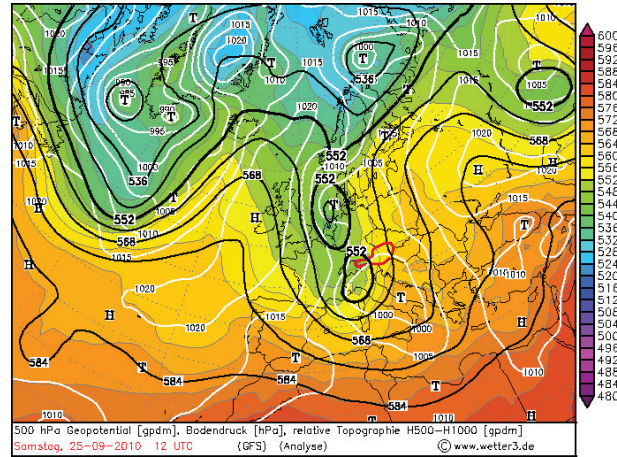


Figure 3.13: Surface pressure and 500 hPa geopotential distribution over Central Europe from GFS at 12 UTC September 25<sup>th</sup>, 2010.

anean Sea, leading to the cyclogenesis near Genoa. This Genoa cyclone travels with the basic flow to the Northwest in a similar path to the so-called Vb cyclone.

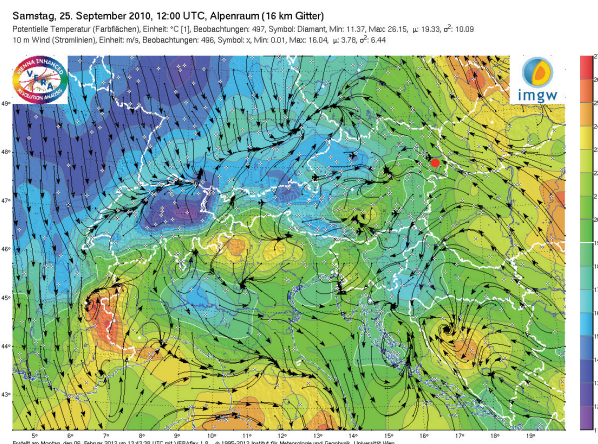


Figure 3.14: Streamlines of 10 m wind and potential temperature from VERA at 12 UTC September 25<sup>th</sup>, 2010.

The passage of the cyclone gives rise to the easterly winds in Eastern Austria, putting the WINDCUBE<sup>TM</sup> in the wake of the wind turbine WEA 4 (figure 2.13).

Under purely easterly winds, the WINDCUBE<sup>TM</sup> at the distance of 2.5 rotor diam-

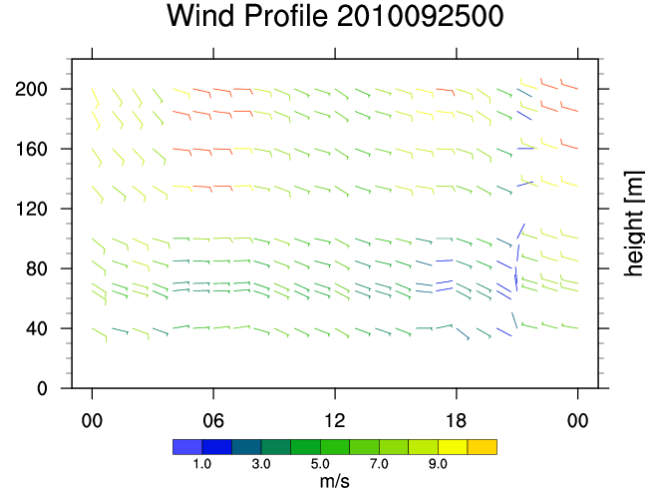


Figure 3.15: Wind profile of September 25<sup>th</sup>, 2010.

eters from the wind turbine is located inside the wake region. Wake effects can be seen in the deceleration of the horizontal wind speed, as well as in increased values for the TKE (figure 3.16).

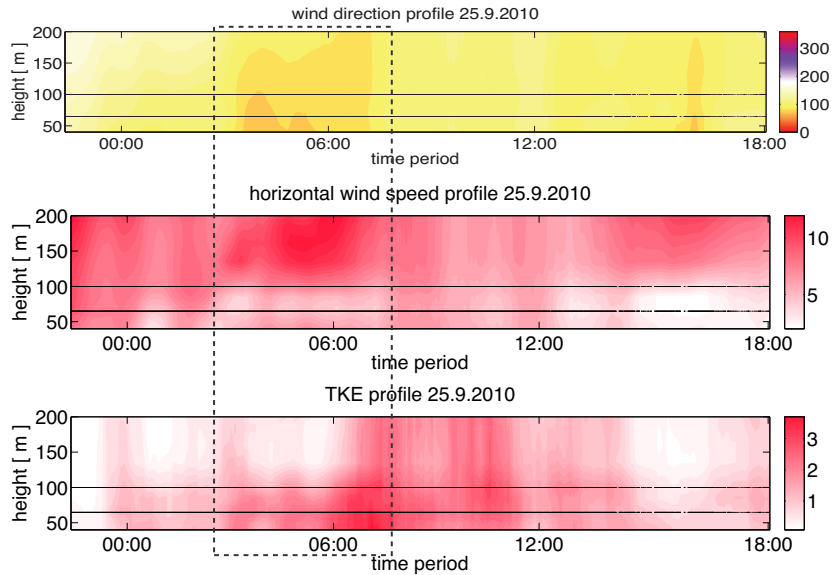


Figure 3.16: Vertical profiles of wind direction [°], horizontal wind speed [m/s] and TKE [ $m^2s^{-2}$ ] on September 25<sup>th</sup>, 2010

The wake of a wind turbine is of a spiral form, with a winding for each rotor blade, that expands with increased distance to the wind turbine (Tong, 2010). In this case, northerly winds near the surface and southerly winds above the blade tip are prevalent (figure 3.17).

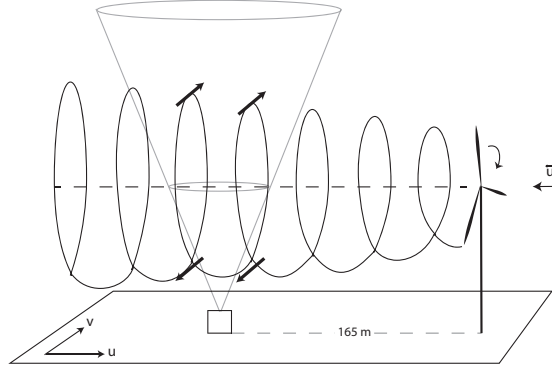


Figure 3.17: Location of the WINDCUBE<sup>TM</sup> in the wake downstream of the wind turbine WEA 4

This is exactly what we find on September 25 between 03 UTC and 08 UTC, as is visualized by the contour plots of the wind components measured by the WINDCUBE<sup>TM</sup> of that day (figure 3.18). As the spiral gets larger with increased distance downstream, the flow reversal does not occur at the height of the blade tip, which is indicated with the horizontal black line at an altitude of 100 m. The second horizontal black line at 65 m indicates the hub height of the wind turbine located next to the device. The flow reversal can be seen in figure 3.18 in altitudes higher than 160 m, at the time interval between 03 UTC and 07 UTC.

Looking at the TKE budget terms, for this case (figure 3.19), it can be seen that different budget terms dominate at different heights. It appears that the largest source of TKE is around the height of the blade tip, indicated by high vertical shear generation near that region. Wind speeds of 13  $m/s$  are decelerated by the turbine, which acts as an obstacle, to 5  $m/s$  (figure 3.19). Near the ground TKE is just redistributed by vertical advection as illustrated in figure 3.19.



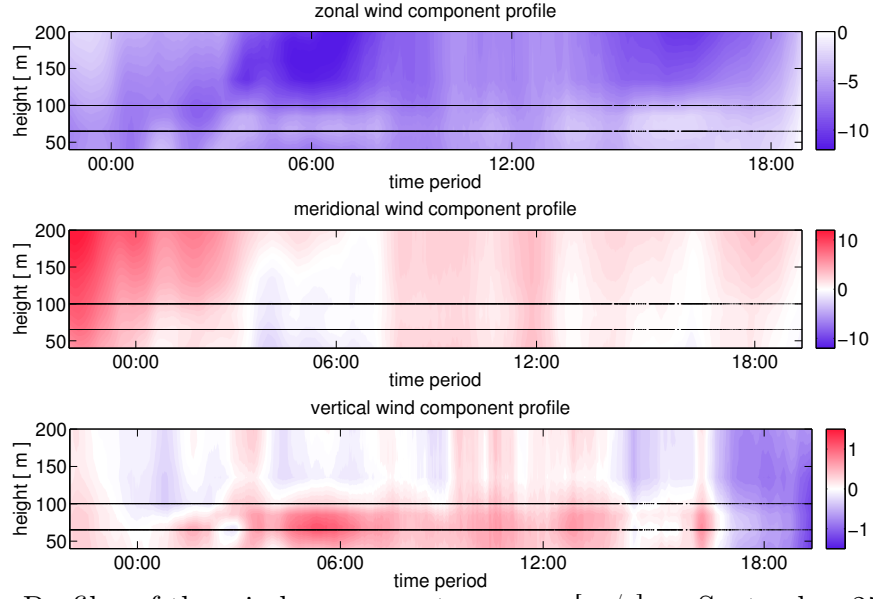


Figure 3.18: Profiles of the wind components  $u$ ,  $v$ ,  $w$  [m/s] on September 25<sup>th</sup>, 2010.

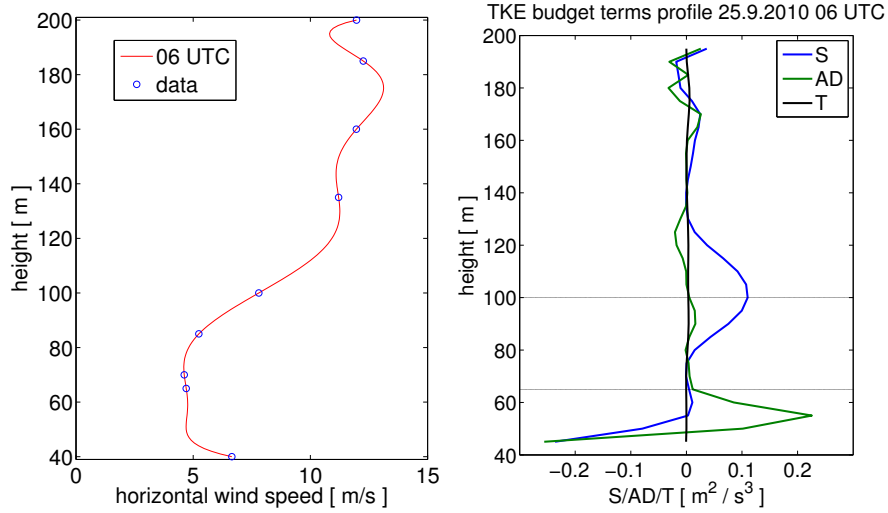


Figure 3.19: Profiles of horizontal wind speed (left) and shear generation  $S$ , vertical advection  $AD$ , tendency  $T$  of the TKE budget (right) at 06 UTC September 25<sup>th</sup>, 2010.



### 3.3.3 Southeasterly (SE) Case

In SE cases the trough axis is located west of Austria bringing mostly warmer and humid air from the Mediterranean Sea. This was the case on October 4<sup>th</sup>, when one of the trough axes lied over France and a strong anticyclone at the surface was located over eastern Europe, which is rather typical for anticyclonic southerly conditions (SA).

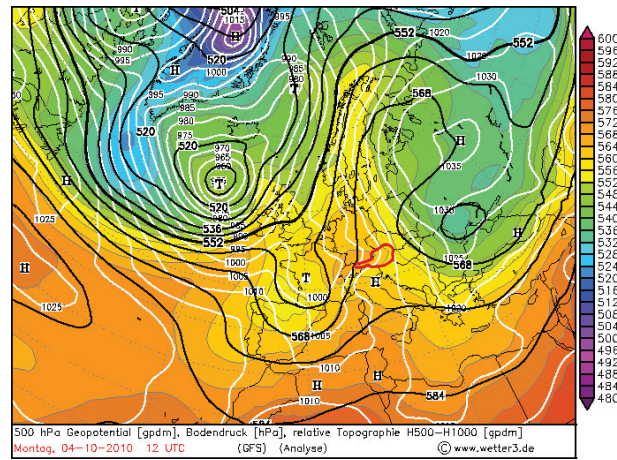


Figure 3.20: Surface pressure and 500 hPa geopotential distribution over Central Europe from GFS at 12 UTC October 4<sup>th</sup>, 2010.

By looking at the 10-m streamlines in the Alpine region (figure 3.21), it can be seen that southeasterly winds predominated over in Eastern Austria. The wind profiles captured by the WINDCUBE<sup>TM</sup> show the same (figure 3.22).

Southeasterly winds in the seasonal transitions are typically associated with high fog, as it indeed happened on this day. The weather station of Vienna also reported sprinkling of rain in the second half of the day <sup>5</sup>. Due to this circumstances a CNR larger than -20 dB was not given throughout the whole day, leading to small data gaps.

<sup>5</sup>Source: [http://ogimet.com/display\\_synops.php?lugar=11035&tipo=ALL&ord=REV&nil=SI&fmt=html&ano=2010&mes=10&day=04&hora=00&anof=2010&mesf=10&dayf=05&horaf=00&enviar=Ver](http://ogimet.com/display_synops.php?lugar=11035&tipo=ALL&ord=REV&nil=SI&fmt=html&ano=2010&mes=10&day=04&hora=00&anof=2010&mesf=10&dayf=05&horaf=00&enviar=Ver), last accessed on February 16<sup>th</sup>, 2012

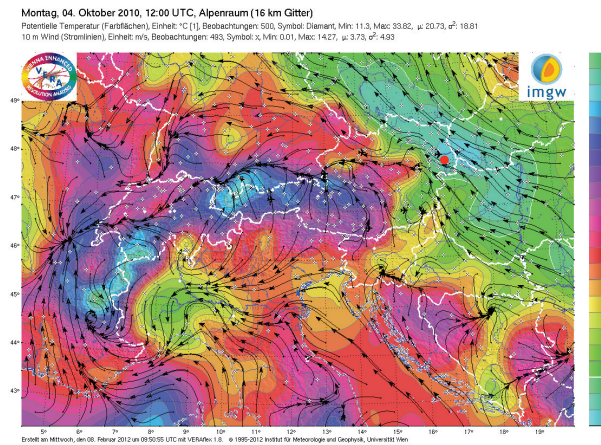


Figure 3.21: Streamlines of 10 m wind and potential temperature from VERA at 12 UTC October 4<sup>th</sup>, 2010.

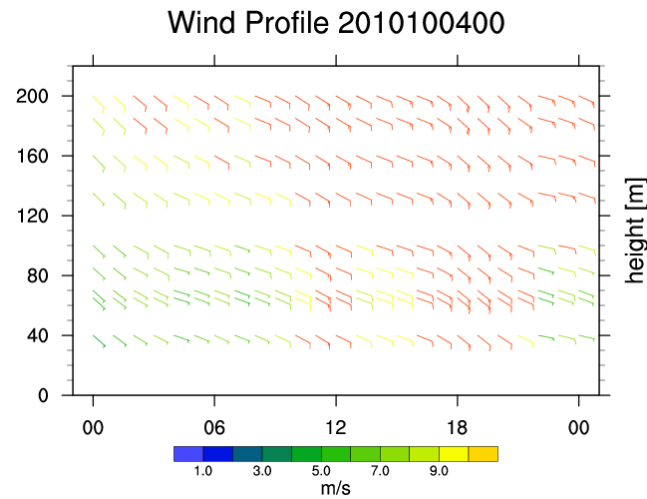


Figure 3.22: Vertical wind profile on October 4<sup>th</sup>, 2010.

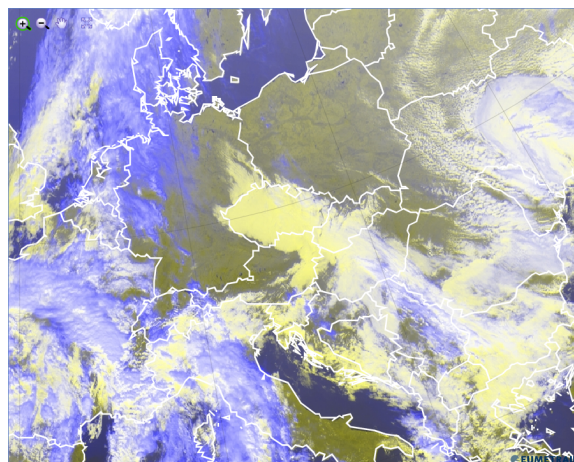


Figure 3.23: Eumetrain HRVIS satellite images at 12 UTC October 4<sup>th</sup>, 2010.

### 3.3. CASE STUDIES

In the course of that day the cyclone, with pressure center over France, moved with the basic flow to the East. Simultaneously, a strong cyclone west of Great Britain approached to the quasi stationary anticyclone over Russia. This resulted in higher pressure differences over Austria and is reflected in the wind speed, as well as in the wind profile over Bruck an der Leithen on that day.

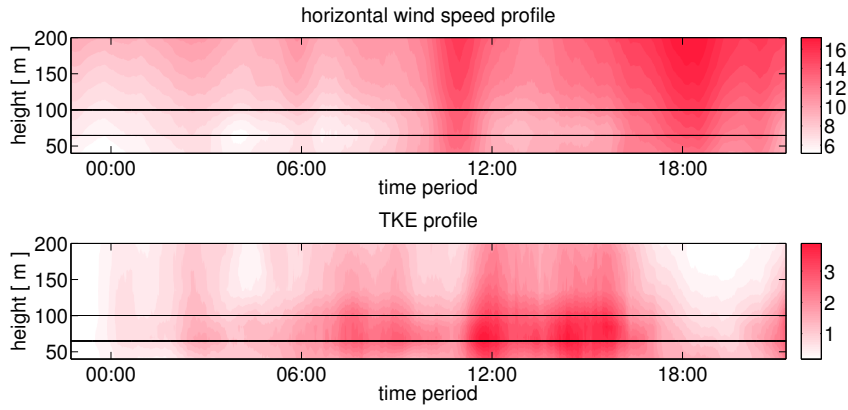


Figure 3.24: Vertical profiles of horizontal wind speed [m/s] and TKE [ $m^2s^{-2}$ ] on October 4<sup>th</sup>, 2010.

Looking at the contour plot of TKE and horizontal wind speed one can see that weak wake effects are present around 6 UTC and 12 UTC, although the flow is not purely from the East. The same features, only weaker in amplitude, are captured in the contour plot of the wind components and in the profile of the TKE budget terms. Although there is no flow reversal in the meridional component, wake effects are visible in the deceleration of the flow downwind of the wind turbine.

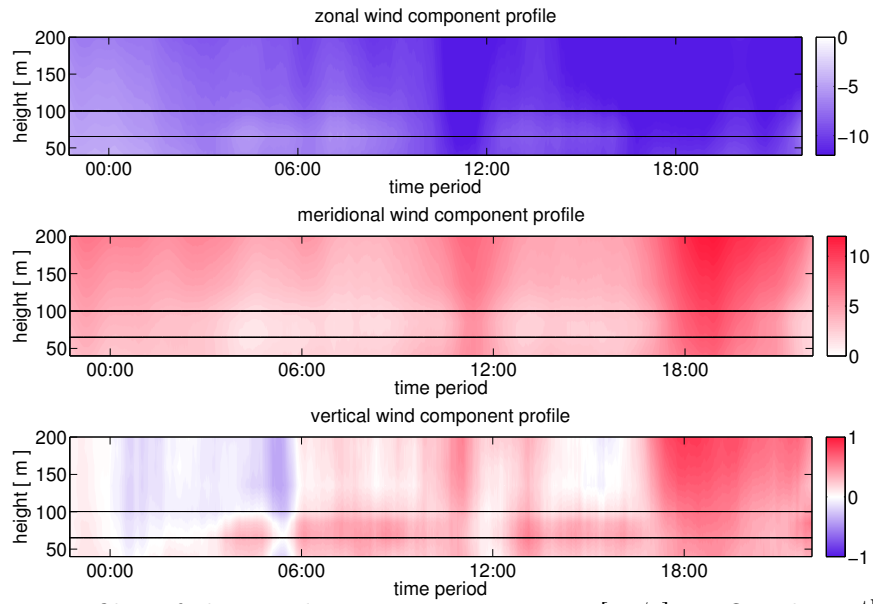


Figure 3.25: Profiles of the wind components  $u$ ,  $v$ ,  $w$  [m/s] on October 4<sup>th</sup>, 2010.

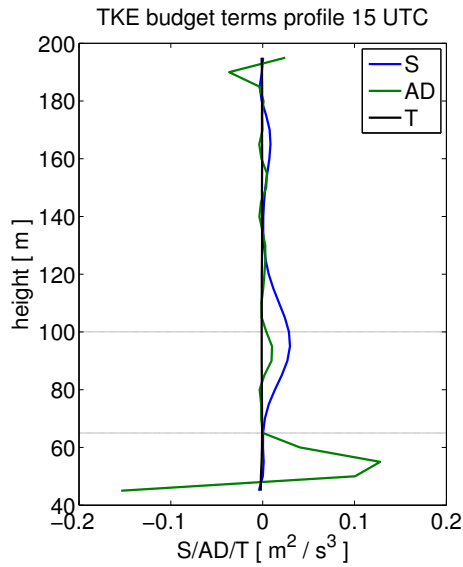


Figure 3.26: Profile of shear generation  $S$ , vertical advection  $AD$  and tendency  $T$  of the TKE budget at 15 UTC October 4<sup>th</sup>, 2010.

### 3.3.4 Northerly (N) Case

An anticyclone over the Norwegian Sea and Fennoscandia is blocking air masses from the Atlantic, which indicates that the HNFZ weather class prevailed on September 5<sup>th</sup>. Therefore, the air masses and the attendant sunny weather conditions stayed the same over Central Europe during that day. The high pressure center located over Norway, together with a region of low pressure over Rumania, produced northwesterly to northerly winds over Eastern Austria. Due to weak pressure gradients wind speeds were also relatively low.

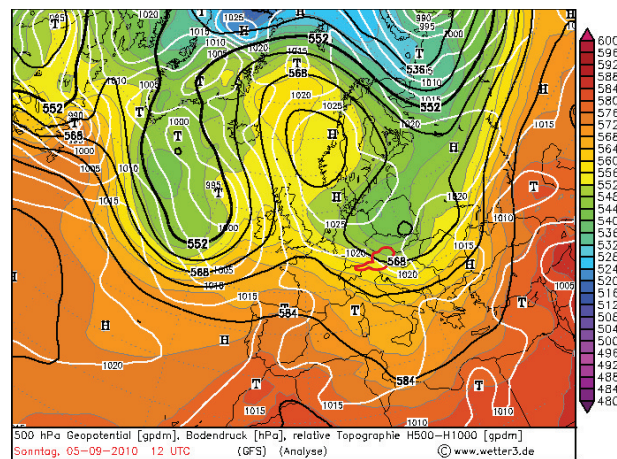


Figure 3.27: Surface pressure and 500hPa geopotential distribution over Europe from GFS at 12 UTC September 5<sup>th</sup>, 2010.

The large-area anticyclone and the low wind speeds provide the ingredients for a convective day, at which the unimpeded incoming solar radiation gives rise to the buoyancy force. This can be seen in the evolution of TKE during the day in figure 3.30.

During the day TKE has a structure of several cells, with the magnitude of around  $3 \text{ m}^2/\text{s}^2$ . Corresponding to these cells, vertical updrafts of around  $1 \text{ m/s}$  (figure 3.31) occur in a period of around an hour or less. In general, the horizontal wind speed shows a similar structure compared to the cells seen in the TKE.

Similar structures of the mean horizontal wind speed can be found when considering a one-dimension simulation of the daily variation of the mean wind from Jansson



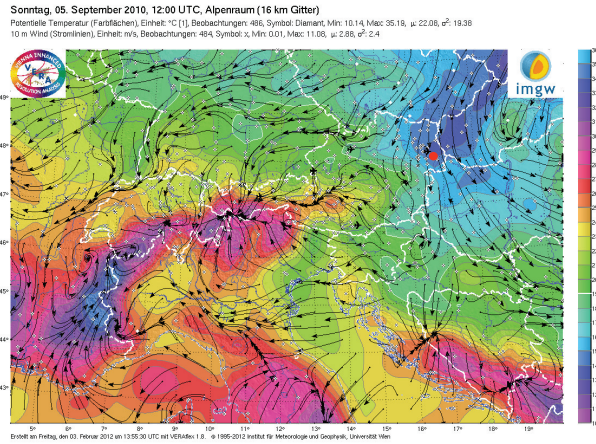


Figure 3.28: Streamlines of 10 m wind and potential temperature from VERA at 12 UTC September 5<sup>th</sup>, 2010.

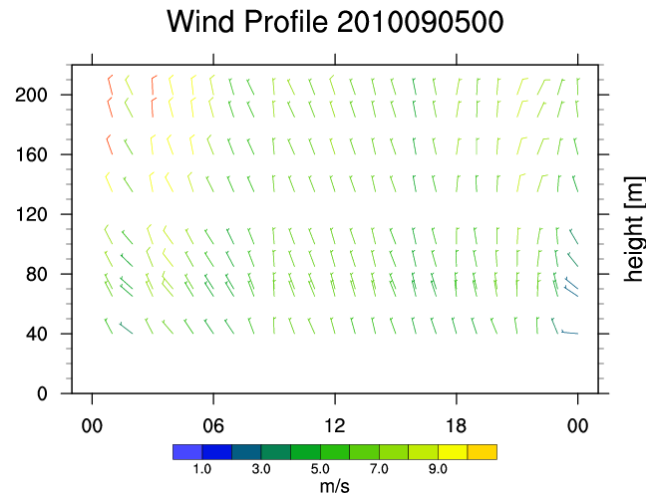


Figure 3.29: Vertical wind profile on September 5<sup>th</sup>, 2010.

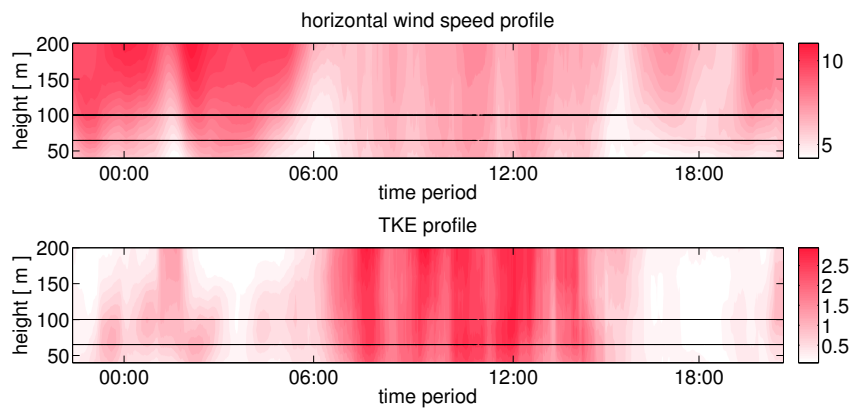


Figure 3.30: Vertical profiles of horizontal wind speed [m/s] and TKE [ $m^2s^{-2}$ ] on September 5<sup>th</sup>, 2010.

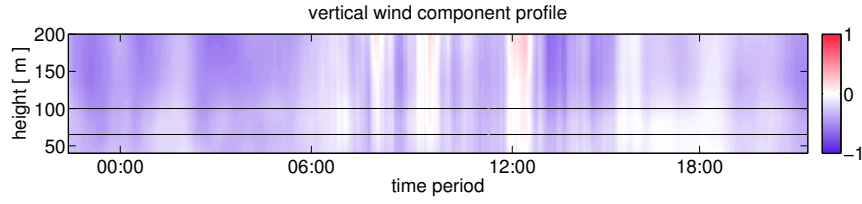


Figure 3.31: Profile of the vertical wind components  $w$  [m/s] on September 5<sup>th</sup>, 2010.

(2002). For the simulation the MIUU mesoscale model was run for a clear August day at 60° North.

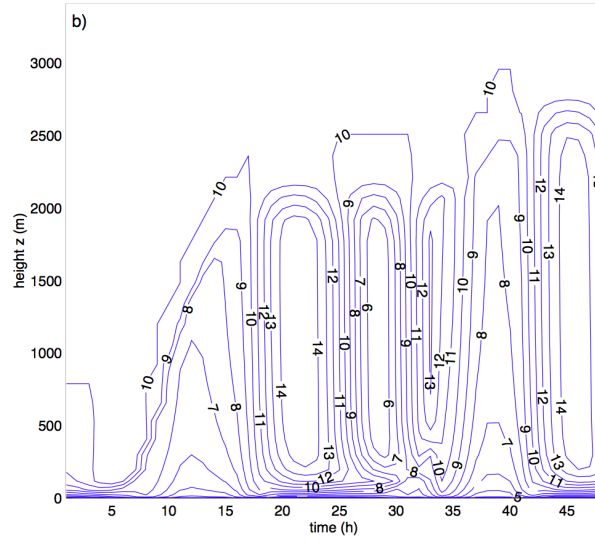
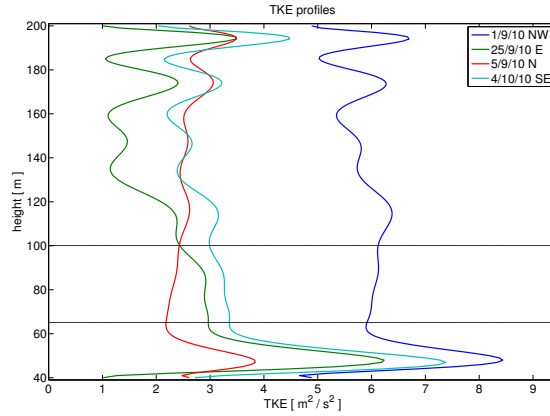


Figure 3.32: Time-height cross section for a 1-D simulation over land with the MIUU mesoscale model, for the diurnal cycle of the mean wind speed (Jansson, 2002)

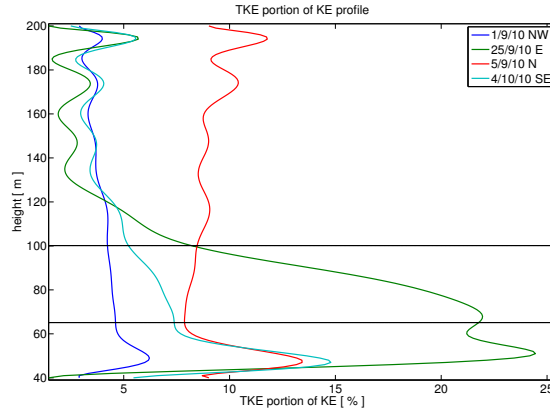
The results shown in figure 3.32 illustrate the daily variations of the boundary layer over land with initially stable atmospheric conditions. One can notice that the cells reach a height of around 2 km, which is by far out of the observation volume of the WINDCUBE<sup>TM</sup>. The cells seem to occur on a timescale of about 5 hours, whereas the observed cells in the case of this study show periods of 1 to 2 hours. These two cases differ in magnitude and structure due to their different location, time of the year and weather condition. Nevertheless, both exhibit the general behavior of a convective boundary layer over land.

### 3.3.5 Comparison of the Case Studies

Comparing the four different cases in terms of TKE shows that not only is the magnitude of TKE of importance but also how large the TKE is with respect to the total kinetic energy (KE) of the flow. The wind turbine cannot convert the TKE because the fluctuations are too large to get the turbine in the correct position in time. Therefore the TKE is a energy loss of the total available energy in the mean flow. To quantify this loss, the TKE portion of the total kinetic energy is plotted for all case studies. Dates with the highest values of the TKE are chosen.



(a) TKE profiles



(b) Profile of the TKE portion of the total kinetic energy

Figure 3.33: TKE profiles and their relation to the total kinetic energy, from case NW at 11 UTC, case N and case SE at 12 UTC and case E at 06 UTC

The highest values of TKE were obtained in the low-level jet NW case and the lowest in the convective N case. Looking at the profiles of TKE portion of the total kinetic



energy, one can see that the highest losses occurred during the E wake case whereas the low-level-jet case had the smallest energy losses due to turbulence. Another interesting feature is TKE being relatively high fraction ( $\sim 10\%$ ) of the total kinetic energy even above the height of the wind turbine in the convective N case. In contrast, in the cases for which shear generation is the main source of TKE, that fraction decrease to 5% above the turbine height.

In general the highest values of turbulence occurred at altitudes between the hub height and the blade tip height, with winds coming from the East (figure 3.33). This is the case in which the WINDCUBE<sup>TM</sup> was located in the wake of the wind turbine. Similar results can be found in terms of turbulence intensity. If plotting turbulence intensity in dependence of wind direction, largest values occurred with easterly winds (figure 3.34). Therefore, the wake of a wind turbine can be characterized by the largest amount of disturbance in the mean flow.

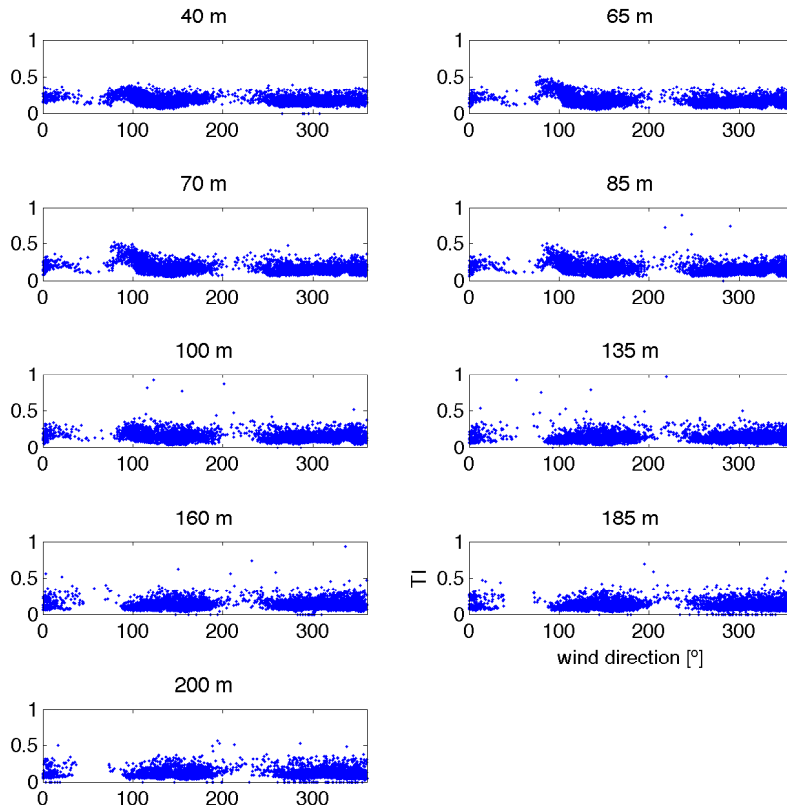


Figure 3.34: Turbulence intensity  $TI$  at different heights as a function of wind direction.

### 3.3. CASE STUDIES

Concerning the representativeness of the weather classes, monthly frequencies of their occurrence over 124 years (1881-2005) are plotted in figure 3.35. On the ordinate, the percent of days in a month is plotted for four different weather classes for all months in a year.

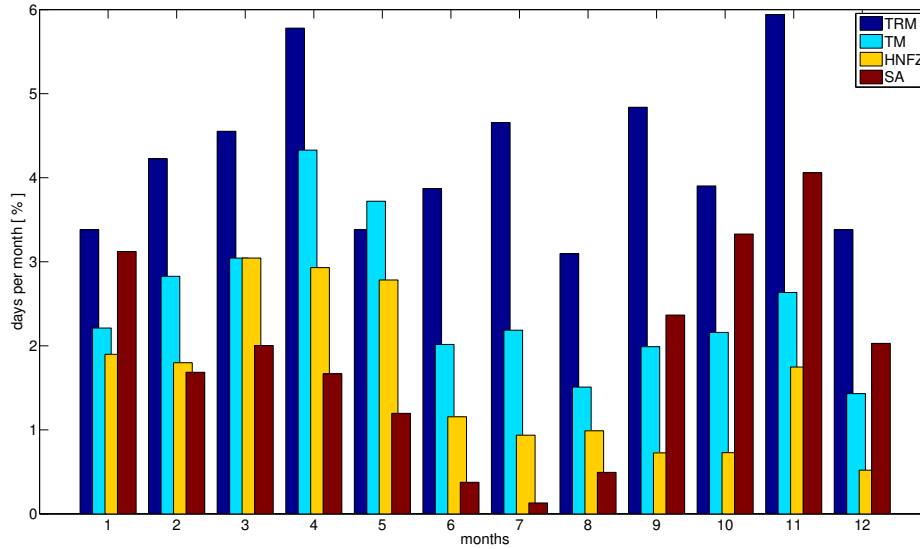


Figure 3.35: Monthly weather class frequencies of the four case studies

The most frequent weather situation is the trough over Central Europe condition, with the highest frequency of occurrence around 6% of the days in April. It is conspicuous that all weather classes have their maxima in spring and autumn. This means that the four weather classes are quite typical for that period of the year, although with a maximum of 5% not as frequent as other classes.

# Chapter 4

## Conclusion

This thesis delivers the analysis of the Doppler LIDAR WINDCUBE<sup>TM</sup> (manufactured by Leosphere) data, collected in a measurement campaign (conducted by VERBUND Renewable Power GmbH) in a wind park near Bruck an der Leitha.

The WINDCUBE<sup>TM</sup> is a ground-base remote sensing device, measuring simultaneously the radial wind speed in the line-of-sight at 9 different altitudes. Care had to be taken of the definition of the coordinate system, as that of the WINDCUBE<sup>TM</sup> differs from the meteorological system. The calculation of horizontal wind speed, wind direction and the three-dimensional wind components lay the base for a meteorological analysis of winds and turbulence in the planetary boundary layer.

As the main focus of this work is on wind energy, turbulence operating processes are discussed in dependence on weather conditions. Turbulent processes are described by variances and covariances of wind parameters, which can be calculated due to a sufficiently high sampling rate (0.25 Hz at one out of 4 measurement points). Therefore, using this raw data set allows an analysis of turbulence through derived parameters such as turbulent kinetic energy (TKE).

The characteristics of the wind field are strongly related to the prevailing weather conditions as, for example, the certain configuration of high and low surface pressure systems over Central Europe leads to a low-level jet over eastern Austria. This low-level jet has a strong mean flow with only a little fraction of TKE. If, in con-

---

trast to this case, the WINDCUBE<sup>TM</sup> is located in the wake of the wind turbine, the fraction of TKE (which cannot be converted to electrical power by the turbines) becomes larger, accounting for almost one quarter of the available kinetic energy of the flow. Referring to the site near Bruck an der Leitha easterly winds are related to the passage of Vb Cyclones, which are with a relative frequency of 6 % of days per month quite common during the seasonal transition time.

Therefor, the design of the wind park should take into the account predominant wind direction as well as the relative frequency of other direction. To take the intensity of turbulence in the wake of turbines into account is of great importance in order to prevent energy losses due to the wake, generated by another wind turbine.

---

# Appendix

## Matlab code for the TKE calculations

```
1 function TKE(daten_2)
2
3 U=daten_2(:,8:8:72);
4 V=daten_2(:,7:8:71);
5 W=daten_2(:,9:8:73);
6
7 h=[daten_2(:,1) -U -V -W];
8
9 %Day
10 start=725136;
11 final=883262;
12 data=h(start:final,:);
13 data(data== -999)=NaN;
14 data(any(isnan(data),2),:)=[];
15 day=data(:,1);
16
17 %Averaging period
18 tp1=600;
19 tp3=300;
20 m=length(data);
21 l=(m./4)-tp1;
22
23 % TKE calculation at 9 different heights
24 for i=1:9
25 data2=[data(:,1) data(:,1+i) data(:,10+i) data(:,19+i)];
26
27 %u-component
28 u1=data2(:,2);
29 n=length(u1);
30 u11=u1(1:4:n); %position 1
31 u12=u1(2:4:n); %position 2
32 u13=u1(3:4:n); %position 3
33 u14=u1(4:4:n); %position 4
34
35 %v-component
36 v1=data2(:,3);
37 v11=v1(1:4:n); %position 1
38 v12=v1(2:4:n); %position 2
39 v13=v1(3:4:n); %position 3
40 v14=v1(4:4:n); %position 4
41
42 %w-component
43 w1=data2(:,4);
44 w11=w1(1:4:n); %position 1
45 w12=w1(2:4:n); %position 2
46 w13=w1(3:4:n); %position 3
47 w14=w1(4:4:n); %position 4
48
49 m=length(w14);
50 %Mean wind components
51 for j=1:m-tp1
52 u11_mean(j)=mean(u11(j:j+tp1));
53 u12_mean(j)=mean(u12(j:j+tp1));
54 u13_mean(j)=mean(u13(j:j+tp1));
55 u14_mean(j)=mean(u14(j:j+tp1));
56
57 v11_mean(j)=mean(v11(j:j+tp1));
58 v12_mean(j)=mean(v12(j:j+tp1));
59 v13_mean(j)=mean(v13(j:j+tp1));
60 v14_mean(j)=mean(v14(j:j+tp1));
61
62 w11_mean(j)=mean(w11(j:j+tp1));
63 w12_mean(j)=mean(w12(j:j+tp1));
64 w13_mean(j)=mean(w13(j:j+tp1));
65 w14_mean(j)=mean(w14(j:j+tp1));
66 end
67
68 M=length(w14_mean);
69
70 %Measurend wind components
71 u11=u11(tp3+1:M+tp3);
72 u12=u12(tp3+1:M+tp3);
73 u13=u13(tp3+1:M+tp3);
74 u14=u14(tp3+1:M+tp3);
75
76 v11=v11(tp3+1:M+tp3);
77 v12=v12(tp3+1:M+tp3);
78 v13=v13(tp3+1:M+tp3);
79 v14=v14(tp3+1:M+tp3);
80
81 w11=w11(tp3+1:M+tp3);
82 w12=w12(tp3+1:M+tp3);
83 w13=w13(tp3+1:M+tp3);
```

```

84 w14=w14(tp3+1:M+tp3);
85
86 %Perturbations of the wind components
87 u11_pert=u11-u11_mean;
88 u12_pert=u12-u12_mean;
89 u13_pert=u13-u13_mean;
90 u14_pert=u14-u14_mean;
91
92 v11_pert=v11-v11_mean;
93 v12_pert=v12-v12_mean;
94 v13_pert=v13-v13_mean;
95 v14_pert=v14-v14_mean;
96
97 w11_pert=w11-w11_mean;
98 w12_pert=w12-w12_mean;
99 w13_pert=w13-w13_mean;
100 w14_pert=w14-w14_mean;
101
102 a11=u11_pert.^2;
103 a12=u12_pert.^2;
104 a13=u13_pert.^2;
105 a14=u14_pert.^2;
106 l=length(a14);
107
108 b11=v11_pert.^2;
109 b12=v12_pert.^2;
110 b13=v13_pert.^2;
111 b14=v14_pert.^2;
112
113 c11=w11_pert.^2;
114 c12=w12_pert.^2;
115 c13=w13_pert.^2;
116 c14=w14_pert.^2;
117
118 for j=1:l-tp1
119     A11(j)=mean(a11(j:j+tp1));
120     A12(j)=mean(a12(j:j+tp1));
121     A13(j)=mean(a13(j:j+tp1));
122     A14(j)=mean(a14(j:j+tp1));
123
124     B11(j)=mean(b11(j:j+tp1));
125     B12(j)=mean(b12(j:j+tp1));
126     B13(j)=mean(b13(j:j+tp1));
127     B14(j)=mean(b14(j:j+tp1));
128
129     C11(j)=mean(c11(j:j+tp1));
130     C12(j)=mean(c12(j:j+tp1));
131     C13(j)=mean(c13(j:j+tp1));
132     C14(j)=mean(c14(j:j+tp1));
133 end
134
135 %MEAN TURBULENT KINETIC ENERGY
136 TKE_1=0.5.*(A11+B11+C11); %position 1
137 TKE_2=0.5.*(A12+B12+C12); %position 2
138 TKE_3=0.5.*(A13+B13+C13); %position 3
139 TKE_4=0.5.*(A14+B14+C14); %position 4
140
141 Y=[TKE_1 TKE_2 TKE_3 TKE_4];
142 TKE_mean1=mean(Y,2);
143
144 %TURBULENCT KINETIC ENERGY
145 TKE11=0.5.*(u11_pert.^2+v11_pert.^2+w11_pert.^2); %position 1
146 TKE12=0.5.*(u12_pert.^2+v12_pert.^2+w12_pert.^2); %position 2
147 TKE13=0.5.*(u13_pert.^2+v13_pert.^2+w13_pert.^2); %position 3
148 TKE14=0.5.*(u14_pert.^2+v14_pert.^2+w14_pert.^2); %position 4
149 TKE11_mean=TKE1(tp3+1:l-tp3);
150 TKE12_mean=TKE2(tp3+1:l-tp3);
151 TKE13_mean=TKE3(tp3+1:l-tp3);
152 TKE14_mean=TKE4(tp3+1:l-tp3);
153
154 Z=[TKE11_mean TKE12_mean TKE13_mean TKE14_mean];
155 TKE__1=mean(Z,2);
156
157 %KINETIC ENERGY
158 KE1=0.5.*((u11.^2)+(v11.^2)+(w11.^2));
159 KE2=0.5.*((u12.^2)+(v12.^2)+(w12.^2));
160 KE3=0.5.*((u13.^2)+(v13.^2)+(w13.^2));
161 KE4=0.5.*((u14.^2)+(v14.^2)+(w14.^2));
162
163 KE1_mean=KE1(1:l);
164 KE2_mean=KE2(1:l);
165 KE3_mean=KE3(1:l);
166 KE4_mean=KE4(1:l);
167
168 X=[KE1_mean KE2_mean KE3_mean KE4_mean];
169 KE__1=mean(X,2);
170
171 %KINETIC ENERGY (MEAN)
172 KE1_mean=zeros(1-tp1,1);
173 KE2_mean=zeros(1-tp1,1);
174 KE3_mean=zeros(1-tp1,1);
175 KE4_mean=zeros(1-tp1,1);

```

```

176 for j=1:l-tp1;
177     KE1_mean(j)=mean(KE1(j:j+tp1));
178     KE2_mean(j)=mean(KE2(j:j+tp1));
179     KE3_mean(j)=mean(KE3(j:j+tp1));
180     KE4_mean(j)=mean(KE4(j:j+tp1));
181 end
182 X=[KE1_mean KE2_mean KE3_mean KE4_mean];
183 KE_mean1=mean(X,2);
184
185 %MEAN KINETIC ENERGY
186 MKE1=0.5.*((u11_mean.^2)+(v11_mean.^2)+(w11_mean.^2));
187 MKE2=0.5.*((u12_mean.^2)+(v12_mean.^2)+(w12_mean.^2));
188 MKE3=0.5.*((u13_mean.^2)+(v13_mean.^2)+(w13_mean.^2));
189 MKE4=0.5.*((u14_mean.^2)+(v14_mean.^2)+(w14_mean.^2));
190
191 MKE1_mean=MKE1(tp3+1:l-tp3);
192 MKE2_mean=MKE2(tp3+1:l-tp3);
193 MKE3_mean=MKE3(tp3+1:l-tp3);
194 MKE4_mean=MKE4(tp3+1:l-tp3);
195
196 X=[MKE1_mean MKE2_mean MKE3_mean MKE4_mean];
197 MKE_mean1=mean(X,2);
198
199 %Portion of TKE of KE
200 anteil1=(TKE_mean1./KE_mean1).*100;
201
202
203 x=[u11_mean u12_mean u13_mean u14_mean];
204 u10_mean=mean(x,2);
205 y=[v11_mean v12_mean v13_mean v14_mean];
206 v10_mean=mean(y,2);
207 z=[w11_mean w12_mean w13_mean w14_mean];
208 w10_mean=mean(z,2);
209
210 x=[u11_pert u12_pert u13_pert u14_pert];
211 u10_pert=mean(x,2);
212 y=[v11_pert v12_pert v13_pert v14_pert];
213 v10_pert=mean(y,2);
214 z=[w11_pert w12_pert w13_pert w14_pert];
215 w10_pert=mean(z,2);
216
217 u1_kurz(:,i)=u11;
218 u2_kurz(:,i)=u12;
219 u3_kurz(:,i)=u13;
220 u4_kurz(:,i)=u14;
221
222 v1_kurz(:,i)=v11;
223 v2_kurz(:,i)=v12;
224 v3_kurz(:,i)=v13;
225 v4_kurz(:,i)=v14;
226
227 w1_kurz(:,i)=w11;
228 w2_kurz(:,i)=w12;
229 w3_kurz(:,i)=w13;
230 w4_kurz(:,i)=w14;
231
232 u0_mean(:,i)=u10_mean;
233 u1_mean(:,i)=u11_mean;
234 u2_mean(:,i)=u12_mean;
235 u3_mean(:,i)=u13_mean;
236 u4_mean(:,i)=u14_mean;
237
238 v0_mean(:,i)=v10_mean;
239 v1_mean(:,i)=v11_mean;
240 v2_mean(:,i)=v12_mean;
241 v3_mean(:,i)=v13_mean;
242 v4_mean(:,i)=v14_mean;
243
244 w0_mean(:,i)=w10_mean;
245 w1_mean(:,i)=w11_mean;
246 w2_mean(:,i)=w12_mean;
247 w3_mean(:,i)=w13_mean;
248 w4_mean(:,i)=w14_mean;
249
250 u0_pert(:,i)=u10_pert;
251 u1_pert(:,i)=u11_pert;
252 u2_pert(:,i)=u12_pert;
253 u3_pert(:,i)=u13_pert;
254 u4_pert(:,i)=u14_pert;
255
256 v0_pert(:,i)=v10_pert;
257 v1_pert(:,i)=v11_pert;
258 v2_pert(:,i)=v12_pert;
259 v3_pert(:,i)=v13_pert;
260 v4_pert(:,i)=v14_pert;
261
262 w0_pert(:,i)=w10_pert;
263 w1_pert(:,i)=w11_pert;
264 w2_pert(:,i)=w12_pert;
265 w3_pert(:,i)=w13_pert;
266 w4_pert(:,i)=w14_pert;
267

```

```
268 TKE_mean(:,i)=TKE_mean1;
269 TKE(:,i)=TKE_1;
270 KE(:,i)=KE_1;
271 KE_mean(:,i)=KE_mean1;
272 MKE_mean(:,i)=MKE_mean1;
273 anteil(:,i)=anteil1;
274 TKE1_mean(:,i)=TKE_1;
275 TKE2_mean(:,i)=TKE_2;
276 TKE3_mean(:,i)=TKE_3;
277 TKE4_mean(:,i)=TKE_4;
278 TKE1(:,i)=TKE11;
279 TKE2(:,i)=TKE12;
280 TKE3(:,i)=TKE13;
281 TKE4(:,i)=TKE14;
282 end
283
284 end
```







Figure 4.2: File sample of the turbulence processed data set

# Bibliography

- Aussibal, C., 2008: *WINDCUBE User's manual*.
- Boquet, J. C. M., 2006-2011: Leosphere pulsed lidar principles. *UpWind*.
- Bourgeois, S. K. S., 2010: Lidar-messung im windpark bruck an der leitha. Tech. Rep. LIDAR-Bericht, Verison 2.0, Meteotest.
- Cebeci, T., 2004: *Analysis of turbulent flows*. Elsevier Inc.
- Friedrich-Wilhelm Gerstengarbe, P. C. W., 2005: Katalog der großwetterlagen europas (1881-2004) nach paul heß und helmut brezowsky. Tech. rep., Potsdamm Institute for Climate Impact Research (PIK).
- Hagen, M., 2010: Einführung in die radarmeteorologie, manuskript zur Vorlesung.
- Hofstetter, C., 2011: Determination of power curve of wind turbines using the remote sensing technology lidar. M.S. thesis, Technische Universität Wien, Fakultät für Elektrotechnik und Informationstechnik.
- Holton, J. R., 2004: *An Introduction to Dynamic Meteorology*. fourth edition ed., Elsevier Inc.
- Jansson, A., 2002: Evaluation of a new lateral boundary condition in the miuu meso-scale model. M.S. thesis, Uppsala University.
- LEOSPHERE, 2008: *WINDCUBE<sup>TM</sup> Product Information*.
- Lotteraner, M. C., 2009: Synoptisch-klimatologische auswertung von windfeldern im alpenraum. Ph.D. thesis, Universität Wien.

- Mayer, D., 2009: Mikrometeorologie, vorlesungsskriptum.
- Neumann, B. C. A. W. T., 2011: Testing the performance of a ground-based wind lidar system. *DEWI Magazin*, **(38)**.
- Pöttschacher, R. S. C. H. W., 2000: A transparent method for analysis and quality evaluation of irregularly distributed and noisy observation data. *Mon. Weather Rev.*, **128**, 2303–2316.
- Richardson, P. M. Y., 2010: *Mesoscale Meteorology in Midlatitudes*. Wiley-Blackwell.
- Stull, R. B., 1991: *An Introduction to Boundary Layer Meteorology*. Kluwer Academic Publishers.
- Tong, W., 2010: *Wind Power Generation and Wind Turbine Design*. WIT Press.
- Tschannett, R. S. M. R. B. B. C. M. D. W. G. C. L. S. S. S., 2006: A mesoscale data analysis and downscaling method over complex terrain. *Mon. Weather Rev.*, **134**, 2578–2771.
- Weitkamp, C., 2005: *Lidar: Range-Resolved Optical Remote Sensing of the Atmosphere*. Springer.
- Werner, I. L. J. S. C., 2001: Virtual doppler lidar instrument. *Journal of Atmospheric and Oceanic Technology*.

# Acknowledgments

First of all, I would like to thank my supervisor Vanda Grubišić for giving me the opportunity of working in a research group and the great guidance during my work for this thesis. I also want to thank Rudolf Zauner and Martin Fink for the great collaboration and the possibility to work with Doppler LIDAR wind data collected by the VERBUND Renewable Power GmbH.

In general I am grateful for the help of Manfred Dorninger and the whole Theoretical Meteorology group at the University of Vienna, especially thanks to Stefano, Michael, Johannes, Lukas and Daniel.

Finally I want to thank my lovely family Waltraud, Alois, Clara, Angela and Anna for the needed support. I would not have achieved this academic step without them.

# Curriculum Vitae

## Personal Details

Main residence	Kirchengasse 20, 7000 Eisenstadt
Secondary residence	Beatrixgasse 25/1/1, 1030 Vienna
Phone	0043 664 5252852
E-mail	valerie-marie.kumer@univie.ac.at
Date of Birth	February 20th, 1989
Nationality	Austria

## Educational History

since 2007	Student of Meteorology at the University of Vienna
Juni 2007	Matura (Higher School Certificate)
1999-2007	BG/BRG/BORG Eisenstadt (secondary school)
1995-1999	Übungsvolksschule Eisenstadt (elementary school)

## Work Experience

Since June 2011	Member of the Theoretical Meteorology group at the Institute of Meteorology and Geophysics in Vienna (IMGW)
SumSem 2011	Tutor of “Feldpraktikum 2”(measurement practical course 2) and “Wetterbesprechung”(weather meeting) at the University of Vienna
February 2010	Meteorological Excursion of the University of Vienna to Costa Rica
WinSem 2010	Tutor of “Feldpraktikum 1”(measurement practical course 1) at the University of Vienna
July/August 2010	Internship at the private weather service UBIMET GmbH

## Conference Contributions

Kumer V., Grubišić V., Dorninger M., Serafin S., Zauner R. (2011) : Analyse von Lidar Winddaten eines Windparks in Bruck an der Leitha. 4th Austrian Meteorology Day, Klagenfurt (AUT), November 3 – November 4, 2011